Microprism-based two-photon imaging of the lateral cortex of the mouse inferior colliculus reveals novel organizational principles of the auditory midbrain.

Baher A. Ibrahim[1,2], Yoshitaka Shinagawa[1, 2], Austin Douglas[4], Gang Xiao[1,2,3], Alexander R. Asilador[2,3,4], & Daniel A. Llano[1,2,3,4,5]

1- Department of Molecular & Integrative Physiology, University of Illinois at Urbana-Champaign, IL, USA.

2- Beckman Institute for Advanced Science & Technology, University of Illinois at Urbana-Champaign, IL, USA.

3- Neuroscience Program, University of Illinois at Urbana-Champaign, IL, USA.

4- School of Molecular & Cell Biology, University of Illinois at Urbana-Champaign, IL, USA.

5- Carle Illinois College of Medicine, University of Illinois at Urbana-Champaign, United States, IL, USA.

Abstract:

To navigate real-world listening conditions, the auditory system relies on the integration of multiple sources of information. However, to avoid inappropriate cross-talk between inputs, highly connected neural systems need to strike a balance between integration and segregation. Here, we develop a novel approach to examine how repeated neurochemical modules in the mouse inferior colliculus lateral cortex (LC) allow controlled integration of its multimodal inputs. The LC had been impossible to study via imaging because it is buried in a sulcus. Therefore we coupled two-photon microscopy with the use of a microprism to reveal the first-ever sagittal views of the LC to examine neuronal responses with respect to its neurochemical motifs under anesthetized and awake conditions. This approach revealed marked differences in the acoustic response properties of LC and neighboring nonlemniscal portions of the inferior colliculus. In addition, we observed that the module and matrix cellular motifs of the LC displayed distinct somatosensory and auditory responses. Specifically, neurons in modules demonstrated primarily offset responses to acoustic stimuli with enhancement in responses to bimodal stimuli, whereas matrix neurons showed onset response to acoustic stimuli and suppressed responses to bimodal stimulation. Thus, this new approach revealed that the repeated structural motifs of the LC permit functional integration of multimodal inputs while retaining distinct response properties.

48 **Introduction:**

49 The inferior colliculus (IC) is a critical integration center in the auditory system (1). The IC
50 comprises a major lemniscal division, the central nucleus (ICC), that receives primarily
51 ascending auditory projections (2-4) and two non-lemniscal divisions known as the dorsal (DC)
52 and lateral (LC) cortices that receive massive descending auditory as well as non-auditory input
53 (5-10) as reviewed in (11). The LC and DC appear to differ in their strategy for integrating these
54 inputs. The DC does not contain known structural heterogeneities but has a tonotopic
55 arrangement of neuronal responses on its surface (12, 13). In contrast, the LC contains
56 repeated neurochemical motifs, here referred to as modules, that express the inhibitory
57 neurotransmitter GABA as well as other metabolic markers (14). Areas outside the modules,
58 referred to as matrix, stain strongly for calretinin (15). We and others have determined that
59 nearly all of the long- and short-range connectivity of the LC is governed by the module/matrix
60 organization (15-18). Unfortunately, how the LC integrates these inputs while maintaining
61 distinct paths of information flow is not known. For example, LC neurons are known to respond
62 to multisensory stimuli (19, 20), but information from different modalities enters the LC in
63 segregated channels (17). Thus, integration across the module/matrix border must occur, but
64 the mechanisms of this integration are unknown. Traditional methods of studying the LC, such
65 as multichannel electrophysiology, pose significant challenges in unambiguously assigning
66 individual recorded neurons to residence in matrix or modules. Imaging approaches, such as
67 two-photon (2P) microscopy, have proven to be enormously valuable in understanding the fine
68 spatial structure of neural response properties in the auditory system (21-23). However,
69 because of its superficial location on the dorsal surface of the mouse midbrain, the DC is the
70 only part of the IC that has been characterized by 2P imaging (12, 13, 24). Optically, it has been
71 impossible to characterize the functions of the LC, which is laterally embedded deep in a brain
72 sulcus. This inability to image the LC impedes our knowledge about how the LC performs the

critical tasks of segregation and integration, whether neurons in the modules or surrounding matrix have different response properties, or whether tonotopy or other spatial structure in response properties exists. Here, we describe a novel approach using a 45º microprism inserted into the sulcus that separates the LC from the cerebellum to investigate the fine-scale functional organization of the LC from its lateral surface through 2P imaging. The 2P images obtained from the microprism revealed the first-ever images of the LC in vivo showing its characteristic GABAergic modules. Compared to the DC imaged from the surface, the acoustically and somatosensory-evoked calcium signals obtained by the 2P imaging of the LC through the microprism revealed functional distinctions between the different cellular motifs of the LC. For instance, while modules were more responsive to somatosensory stimulation than matrix, the latter was more acoustically-responsive and had a lower detection threshold for complex sounds. Additionally, modules and matrix were found to differently process the spectral and temporal features of the acoustic information. These findings suggest that the non-lemniscal divisions of the IC contain rich but distinct platforms for the processing of different features of auditory information as well as multisensory integration.

Results:

The insertion of 45º microprism for imaging the LC from the side.

GAD67-GFP knock-in mice on a Swiss Webster background were crossed with Thy1-jRGECO1a mice to produce a GAD67-GFPx jRGECO1a hybrid mouse, which was used to visualize GABAergic modules, to identify the dense network of GABAergic neurons and terminals in modules of the LC in the green channel (25), and the calcium indicator, jRGECO1a, in the red channel (26). A standard craniotomy was performed (27) with modifications to suit the specific characteristics of the IC in terms of its location, depth, and high density of the surrounding vasculature (28). The craniotomy (~ 3 x 4 mm) did not drill directly into the sagittal and lambdoid sutures which allowed minimal disruption of the superficial sinuses below the skull

98 (Figure 1A) as indicated by the minimal bleeding near the bone flap (Figure 1B). During drilling,
99 pressurized air and a cold stream of saline were used to remove the bone debris and dissipate
100 heat. Because the IC sits deeper in the brain compared to the surrounding structures, the direct
101 insertion of the 45° microprism was found to push the IC ventrally. Therefore, a fine diamond
102 knife was used to separate the lateral surface of the IC from the surrounding tissues without
103 damaging the transverse and sigmoid sinuses (Figures 1C and D). This step was followed by a
104 gentle retraction of the knife medially to generate a pocket to secure the microprism (Figure 1E).
105 The successful insertion of the microprism was assessed by examining the reflection of the
106 diamond knife from the microprism's top glass surface (Figures 1F and G). Holding the
107 microprism down and retracting the knife upward simultaneously resulted in securing the
108 microprism in its pocket (Figure 1H). Locking the microprism down in its pocket for 10 minutes
109 with the diamond knife (Figure 1J) is critical to ensure that the microprism is stabilized and to
110 prevent bleeding. Filling the gap between the skull surface and the microprism with saline was
111 found to generate motion artifact due to the heart pulsation, so 1% agarose was used to fill the
112 gap to reduce the motion artifact and add more stability to the microprism (Figure 1K). To
113 compare response properties between the LC and DC, direct imaging (i.e., without a
114 microprism) of the dorsal surface of the IC, where the DC is located, was also conducted by
115 scanning the DC surface from the most medial to lateral regions following the convex curvature
116 of the surface (Figures 1L and M).

117 **The 2P characterization of GABAergic and non-GABAergic neuronal distribution on the**
118 **LC and DC surfaces with histological validation.**

119 Following the surgery, the anesthetized animals were taken immediately for imaging.
120 Examination of the distribution of GABAergic modules in the LC was critical to validate the
121 target area for functional calcium imaging. Therefore, the 920 nm laser beam was initially used
122 to scan for GFP, which is expressed in the GABAergic cells of GAD67-GFP knock-in mice. The

123 insertion of the microprism was initially viewed by low magnification epifluorescence imaging of
124 the GFP signals from the whole surface of the IC along with the inserted microprism (Figure
125 2A). This step validated the location of the microprism relative to the IC under the microscope
126 and ensured there was no bleeding that could block the field of view. The 2P images of the GFP
127 signals from the LC imaged via the microprism (Figures 2C and E, the irregular white lines)
128 across different animals revealed the LC characteristic GABAergic modules, which were
129 consistent with previous 3D reconstructions of modules from the coronal sections (14, 17). To
130 further validate the microprism location and the ability to image the LC from the lateral surface,
131 a laser lesion (see Methods) was created via the microprism (Figure 3A), which was validated
132 histologically (Figure 3B). For comparison, the whole dorsal surface of the IC was scanned from
133 medial to lateral borders (Figure 2B, the dotted white lines). Unlike the LC, most of the dorsal
134 surface of the IC showed a non-clustered distribution of the GABAergic cells (Figures 2D and F,
135 blue boxes). However, the lateral horizon of the IC dorsal surface showed clusters of
136 GABAergic cells and terminals that were confirmed to be modules, which comprise the
137 prominent feature of the LC (Figures 2D and F, red boxes). To further validate the presence of
138 GABAergic modules in the dorsolateral surface of the IC, a laser lesion was created in a
139 GABAergic module located in that area (Figures 3C and D), which was confirmed histologically
140 (Figure 3E), demonstrating that it is possible to image a portion of the LC directly from its dorsal
141 surface.

142 Using the 1040 nm laser, the GAD67-GFPx jRGECO1a hybrid mouse showed a non-clustered
143 cellular expression of jRGECO1a on the surface of the DC (Figure 4A) or on the surface of the
144 LC imaged via microprism (Figure 4B), as expected. The IC of anesthetized animals in each
145 experimental setup was then imaged to measure calcium signals over the course of
146 pseudorandom presentations of either 500 ms pure tones of different combinations of
147 frequencies (5-40 kHz, half octave intervals) and sound levels (40-80 dB SPL, 10 dB intervals)

148 or broadband noise without or with amplitude modulation (AM-noise) of different combinations of
149 AM frequencies (2-256 Hz, one-octave intervals) and sound levels (40-80 dB SPL, 10 dB
150 intervals). As shown by two representative cells from the DC imaged from the dorsal surface or
151 LC imaged via microprism, these acoustic stimulation paradigms successfully elicited transient
152 cellular calcium signals that varied depending on the stimulus type (Figures 4C and D).

153 **The auditory cellular organization of the LC via microprism versus the DC.**

154 As indicated by the GFP signals and consistent with Figure 2, imaging the LC of the hybrid mice
155 via microprism showed clusters of GABAergic modules, which take different irregular shapes on
156 the surface of the LC (Figure 5A - irregular white lines). Based on the best pure tone frequency
157 of each responsive cell (13), an inconsistent and fragmentary tonotopic organization was seen
158 over the LC imaged via microprism (Figure 5B). For comparison, the surface of the DC was
159 imaged directly from the dorsal surface using the routine imaging setup. To view the majority of
160 the DC surface, imaging was done by scanning the DC from its medial to the lateral horizon to
161 generate a composite map (see Methods). As indicated by the GFP signals, it was noted that
162 the most lateral region of the surface of the IC showed clusters of the GABAergic cells and
163 terminals (i.e., modules, Figure 5C – irregular white lines) and are therefore considered part of
164 the LC. Based on the best pure tone frequency of each responsive cell (13), the DC showed a
165 tonotopic organization of cells along the rostromedial to caudolateral axis tuned to lower or
166 higher frequencies, respectively (Figure 5D). This tonotopic organization is similar to those
167 previously described (12, 13). It was also noticed that a large area of the DC was tuned to the
168 lowest tested frequency (5kHz), which could indicate a bias to the low frequency on the surface
169 of the DC. To quantify tuning differences between DC and LC, the cumulative distribution
170 function based on the cells' best frequency showed a low-frequency bias in the DC, similar to
171 previous work (24, 29-31), while most of the LC cells imaged via microprism were tuned to

172 higher frequencies (Figure 5E, Mann-Whitney Test: $z = -10.5$, $p < 0.001$, a median of best-tuned
173 frequency = 5 and 7.1 Hz for DC and LC via microprism, respectively).

174 Detection of AM is critical to identify natural sounds as well as to aggregate sound sources
175 during auditory scene analysis, which is important for communication (32-34). The IC also is the
176 first site in the ascending auditory pathway where a substantial number of neurons are rate-
177 tuned to AM (32, 35-38). Even though calcium indicators do not provide a spike-by-spike
178 readout of neural activity, their integrated signal does correlate with the number of spikes
179 produced by a neuron over short time windows (39, 40). Thus, this integrated signal can be
180 used to measure rate responses to AM. Using this integrated signal, we tested the ability of the
181 cells of LC imaged via microprism in its different motifs to respond to broadband noise at
182 different AM rates. We observed a significant fraction of cells that did not respond to pure tones
183 responded to AM-noise (Figure 6A, paired-sample t-test: $t_{(6)} = -11.13$, $p = 3.1\times10^{-5}$, the
184 percentage of responsive cells mean ± SEM = 34.7 ± 9.2% and 56.2 ± 8.9% for pure tones and
185 AM-noise, respectively). We also observed that modules and matrix differentially process the
186 temporal information. For instance, the matrix had a significantly greater fraction of cells that
187 respond only to AM-noise compared to the modules (Figure 6B – striped blue bar, Mann-
188 Whitney Test, $p = 0.02$), which suggests that neurons in the matrix are more sensitive to
189 complex sounds compared to those in the modules. In contrast, both cellular motifs had similar
190 fractions of cells that are responsive to pure tones (Figure 6B – solid blue bar, Mann-Whitney
191 Test, $p = 0.58$). These findings suggest that neurons in the matrix are more responsive to
192 sounds of greater spectral and temporal complexity than those in the modules. In the DC, like
193 the LC imaged via microprism, a significant fraction of cells that did not respond to pure tones
194 did respond to AM-noise (Figure 6C, paired samples t-test: $t_{(3)} = -5.8$, $p = 0.01$, the percentage
195 of responsive cells mean ± SEM = 78.4 ± 3.6% and 97.3 ± 0.4% for pure tones and AM-noise).

196 Regardless of the sound type, animals showed a lower fraction of responsive neurons to the
197 acoustic stimulation in the LC imaged via microprism compared to DC (pure tone: two-sample t-
198 test, $t_{(9)} = 2.9$, $p = 0.02$, the percentage of responsive cells mean ± SEM = 78.5±11.0% and
199 35.0±9.2% for DC and LC, respectively, AM-noise: two-sample t-test, $t_{(9)} = 3.5$, $p = 0.007$, the
200 percentage of responsive cells mean ± SEM = 98.1±1.7% and 56.3±8.8% for DC and LC,
201 respectively). To evaluate if any optical artifacts due to imaging through a prism could be
202 responsible for this finding, the number of responsive cells imaged from the lateral-most dorsal
203 surface of the IC, which we consider part of the LC because of the presence of GABAergic
204 modules (LC imaged from the dorsal surface), was quantified and compared with that obtained
205 from the LC imaged via microprism. We observed that there were no significant differences
206 between the number of tone or noise-responsive neurons between the LC imaged via
207 microprism or directly from the dorsal surface (pure tone: two-sample t-test, $t_{(9)} = 1.1$, $p = 0.28$,
208 AM-noise: two-sample t-test, $t_{(9)} = 1.6$, $p = 0.14$).

209 **LC and DC have different spectral and temporal modulation indices.**

210 Given that more cells from LC imaged via microprism and DC had responses to AM-noise
211 compared to pure tones, we further quantified the selectivity to spectral or temporal modulation
212 by computing the spectral modulation index (SMI) or the temporal modulation index (TMI),
213 respectively, for all the responsive cells (see Methods) across the tested sound levels.

214 For the LC imaged via microprism, the LC matrix has a greater proportion of spectrally
215 modulated cells than modules most prominently at sound levels below 70 dB (Figure 7A, two-
216 way ANOVA: $p = 7.1\times10^{-7}$, 1.0, and 0.01 for the region, sound level, and interaction,
217 respectively, the percentage of modulated cells mean ± SEM for modules vs. matrix) suggesting
218 that the cells in the matrix have a lower threshold to detect complex spectral features of sound.
219 Similarly, the matrix had more cells responsive to temporal modulation as a main effect (Figure

220 7B, two-way ANOVA, $p = 7.1 \times 10^{-7}$, 1.0, and 0.32 for the region, sound level, and interaction,
221 respectively), which was consistent with the above results (Figure 6B).

222 The DC and LC imaged via microprism were found to have different profiles of modulation of
223 responses to spectral and temporal complexity. Although there is a general trend for SMI and
224 TMI to decrease with increasing sound-pressure level, corresponding to an increase in pure-
225 tone responsiveness, overall there is a statistically-significant higher level of average SMI and
226 TMI in the LC compared to the DC (Figures 7C and D, SMI: two-way ANOVA, $p < 0.001$ for all
227 region, sound level, and interaction, TMI: two-way ANOVA, $p < 0.001$ for all regions, sound
228 level, and interactions). These results suggested that neurons in the LC are more sensitive to
229 spectral and temporal modulation than those in the DC.

230 **The somatosensory vs. auditory responses over the LC imaged via microprism.**

231 Somatosensory inputs from many cortical and subcortical structures have been identified in the
232 non-lemniscal division of the IC, particularly in the LC (17, 19, 41) Previous work has shown
233 that while somatosensory projections mostly target the modules, the auditory projections tend to
234 target the matrix (17), which indicates that the LC is a multisensory integration site. Therefore,
235 we examined the somatosensory and auditory cellular responses on the surface of the LC by
236 coupling the two-photon imaging with the microprism with a whisker or acoustic stimulation (see
237 Methods). Acoustic stimulation was done with 500 ms broadband noise at 80 dB SPL. After the
238 acoustic or somatosensory stimulation, evoked cellular responses were observed from the LC
239 neurons imaged via microprism either at the beginning of the stimulation (Figures 8A and B –
240 onset responses) or at the termination of the stimulation (Figures 8C and D – offset responses).

241 Auditory and somatosensory responses were evoked in the neurons of both matrix and modules
242 imaged via microprism (Figures 9A, B, D) and the cells were categorized within each motif into
243 cells that respond only to acoustic stimulation, only to somatosensory stimulation, or to both

244 stimuli (Figure 9F). The quantification of the percentage of cells in both modules and matrix
245 revealed that the percentage of responsive cells to sound only was higher than that of cells
246 responsive to somatosensory stimulation or those responsive to both stimuli with no preference
247 (Modules: Figure 9H, one-way ANOVA, $p = 4.0x10^{-5}$, the percentage of responsive cells mean ±
248 SEM = 41.9 ± 5.4% (auditory-only response), 4.2 ± 0.8% (somatosensory-only response), and
249 10.2 ± 1.4% (auditory + somatosensory responses)) (Matrix: Figure 9I, One-way ANOVA, p =
250 $2.4x10^{-4}$, the percentage of responsive cells mean ± SEM = 43.7 ± 8.5% (auditory response),
251 0.88 ± 0.36% (somatosensory response) and 2.9 ± 0.34% (auditory + somatosensory
252 responses)). However within the pool of responsive cells and normalized against modules, we
253 observed that more sound-responsive cells were found in the matrix, while more somatosensory
254 responsive cells were found in the modules (Figures 9B, D, F, and J, Mann-Whitney Test, p =
255 0.028, Mann-Whitney Test, p = 0.028), which was consistent with the reported difference in
256 inputs to modules compared to matrix (17). Most of the acoustically-responsive cells in the
257 matrix showed onset responses, and the cells showing acoustically-driven offset responses
258 were clustered in the modules (Figures 9C and K, onset response: Mann-Whitney Test, p =
259 0.028, offset response: Mann-Whitney Test, p = 0.028).

260 Additionally, most of these auditory-offset cells were also responsive to somatosensory
261 stimulation as shown by the merged responses (Figure 9F), which suggests a multisensory
262 integrative function by those cells as discussed later. Given the specific spatial location of the
263 somatosensory-responsive cells in the modules which contain clusters of GABAergic cells, we
264 asked if somatosensory stimulation could suppress the auditory response when both stimuli are
265 presented simultaneously (bimodal stimulation). To test this hypothesis, we calculated and
266 visualized the response index (RI), which was calculated as the ratio of the cellular response to
267 bimodal stimulation to the cellular response to acoustic response alone for auditory-responsive
268 cells. We observed that cells in the modules had a higher odds of having an enhancement

response to bimodal stimulation than matrix, while cells in the matrix had a higher odds of having a suppressive response to bimodal stimulation (Figures 9G and L, enhanced response: Mann-Whitney Test, $p = 0.028$, matrix median odds = 0.68, suppressed response: Mann-Whitney Test, $p = 0.028$, matrix median odds = 1.33).

Consistent with the above data, the LC imaged from the dorsal surface (Figures 10A-D, dorsolateral) shared common response profiles with the LC. For instance, the LC imaged via microprism or directly from the dorsal surface had a higher percentage of somatosensory responsive cells than the DC (Figure 10A-D, dorsal and dorsomedial) as quantitatively shown (Figure 10H, one-way ANOVA, $p = 0.02$, the percentage of somatosensory responsive cells mean ± SEM = 1.3 ± 0.83% (DC), 8.2 ± 2.4% (LC imaged from the dorsal surface), and 8.1 ± 0.64% (LC imaged via microprism), which suggest that the LC is the main region of the IC shell that processes somatosensory information, consistent with the anatomical reports (17, 20, 42, 43). The matrix of the LC imaged from the dorsal surface had more responsive cells to sound (Figures 10E and I, Mann-Whitney Test, $p = 0.028$, the matrix:module median ratio = 1.5), and less responsive cells to somatosensory stimulation compared to its modules (Figures 10E and I, Mann-Whitney Test, $p = 0.028$, matrix:module median ratio = 0.28). Additionally, more acoustically onset responsive cells were found in the matrix (Figures 10F and J, Mann-Whitney Test, $p = 0.028$, matrix:module median ratio = 10.2), while more acoustically offset responsive cells were found in the modules (Figures 10F and J, Mann-Whitney Test, $p = 0.028$, matrix:module median ratio = 0.02). More acoustically responsive cells in the matrix displayed suppressed responses following the bimodal stimulation (Figures 10G and K, Mann-Whitney Test, & $p = 0.028$, matrix:module median ratio = 1.5). In contrast, more acoustically responsive cells in the modules displayed enhanced responses following the bimodal stimulation (Figures 10G and K, Mann-Whitney Test, & $p = 0.028$, matrix:module median ratio = 0.42). These data

293 confirmed the findings obtained from the LC imaged via microprism and emphasized the
294 functional difference between the LC and DC.

295 **The acoustic and somatosensory response from LC imaged via microprism and DC**
296 **imaged from the dorsal surface in awake animals.**

297 To determine if the presence of ketamine/xylazine anesthesia influenced the response
298 properties detailed above, additional experiments were performed in awake animals (n=5 total,
299 3 from LC using prism and 2 from dorsal surface). Similar to what was observed under
300 anesthesia, the cells of the LC imaged via microprism did not show clear evidence for tonotopy
301 (Figure 11B). In contrast, the data obtained from imaging the DC under awake preparations
302 showed a similar tonotopic map (Figure 11D) as that observed under anesthesia, though a
303 greater proportion of high-frequency cells were observed leading to the observation of a low-
304 frequency border similar to the previous under awake preparations (12). Similar to the results
305 obtained under anesthesia, the LC imaged via microprism had more cells tuned to higher
306 frequencies compared to the DC (Figure 12A, Mann-Whitney test, $p<0.001$, a median of best-
307 tuned frequency = 10 and 5 kHz for LC and DC, respectively). Both LC imaged via microprism
308 and DC imaged directly from its dorsal surface were more responsive to AM-noise than pure
309 tones (Figure 12B, DC: χ^2 test = 72.73, $p< 0.001$, the percentage of responsive cells = 69.2 vs.
310 85.8% for pure tone vs. AM-noise, respectively, LC: χ^2 test = 43.6, $p = 1.8\times10^{-9}$, the percentage
311 of responsive cells = 58.7 vs. 76.1% for pure tone vs. AM-noise, respectively). Within the
312 responsive cells population, the DC was found also to have more responding cells to sound
313 either pure tone or AM-noise compared to the LC imaged via microprism (Figure 12C, pure
314 tone: χ^2 test = 17.8, $p = 4.8\times10^{-4}$ the percentage of responsive cells = 62.9 vs. 37.1% for DC vs.
315 LC, respectively, AM-noise: χ^2 test = 23.6, $p = 2.9\times10^{-5}$ the percentage of responsive cells =
316 61.9 vs. 38.1% for DC vs. LC, respectively). Additionally, the matrix also showed more
317 responsive cells to sound compared to the modules regardless of the stimulus type (Figure 12D,

318 pure tone: χ^2 test = 31.9, p = 5.2×10^{-7}, the percentage of responsive cells = 30.8 vs. 69.2% for
319 modules vs. matrix, respectively, AM-noise: χ^2 test = 11.1, p = 0.01, the percentage of
320 responsive cells = 37.6 vs. 62.4% for modules vs. matrix, respectively).

321 For somatosensory responses, similar to the anesthetized preparation, neurons in modules
322 imaged via microprism had more cells responsive to somatosensory stimulation than the matrix,
323 while the latter had more responsive cells to broadband noise (Figures 13A, C, E, and G,
324 auditory response: χ^2 test = 31.9, p = 5.2×10^{-7}, the percentage of responding cells = 22 vs. 78%
325 for modules vs. matrix, respectively, somatosensory response: χ^2 test = 11.1, p = 0.01, the
326 percentage of responding cells = 63.6 vs. 36.4% for modules vs. matrix, respectively). Similar to
327 anesthetized data, we found that most of the auditory responsive cells in the modules and
328 matrix had suppressed auditory responses following bimodal stimulation (Figures 13F and H, χ^2
329 test = 31.9, p = 5.2×10^{-7}, matrix: The percentage of responding cells = 69.6 vs. 30.4% for
330 suppressed vs. enhanced responses, respectively, modules: The percentage of responding
331 cells = 95 vs. 5% for suppressed vs. enhanced responses, respectively), indicating an overall
332 suppression in the cellular auditory response.

333 **Discussion:**

334 *Summary:*

335 As a new imaging approach, a microprism was used to image the LC surface, which is hidden in
336 a brain sulcus, to provide the first-ever sagittal image of the LC in vivo and to examine its
337 functional organization, which revealed the functional distinction between the LC imaged with
338 microprism and DC imaged directly from the dorsal surface. Imaging the LC either via
339 microprism or from the dorsal surface revealed that it contains repeated cellular motifs as
340 clusters of GABAergic cells and terminals forming irregular shapes called modules that were
341 embedded in areas of mostly non-GABAergic cells called matrix. Although modules and matrix

342 were found to be activated by somatosensory and auditory stimuli, they were functionally
343 distinct. The matrix had more auditory-responsive cells with a lower threshold for complex
344 sound detection and had more cells processing complex spectral and temporal auditory features
345 than modules. In contrast, modules had more somatosensory responsive cells, which was
346 consistent with the previously-described anatomical differences in input to the modules
347 compared to matrix (17). Somatosensory stimulation was found to suppress the auditory
348 response in the matrix, which suggests that multisensory interactions exist between the matrix
349 and modules. These findings indicate that the LC specifically processes multisensory
350 information, which is a critical functional distinction between the LC and DC. Despite the ability
351 of DC and LC to extract the basic spectral features of auditory information, more cells in the LC
352 and DC were responsive to AM-noise than pure tone, which fits the function of the IC shell as a
353 nonlemniscal division. The spectral and temporal modulation of the LC and DC were found to be
354 more pronounced at lower sound levels, which could help in acoustic object detection in noisy
355 environments. However, the LC was generally more responsive to sounds with greater spectral
356 and temporal complexity than those in the DC.

357 *The novelty of the imaging setup and technical considerations*

358 Given its ability to reflect the light at its hypotenuse, microprism-based 2P- microscopy has been
359 successfully used to image the six cortical layers in the somatosensory and visual cortices of
360 mice (44) and to image other inaccessible cortical surfaces like those folded in the brain sulci
361 such as the medial prefrontal cortex (45) or entorhinal cortex (45-47). In those studies, the glass
362 window glued to the microprism was used, which requires significant skill and potential removal
363 of brain regions to allow prism access (46). Another approach is to use a micro metal or
364 diamond-made knife to create a pocket with minimal tissue damage (44, 48). Accordingly, we
365 combined and modified some of these procedures to improve the microprism implantation to

image the sagittal surface of the LC, which is deeply embedded into the brain tissue in a highly vascular area, with minimum damage to the IC or the surrounding vasculature.

Previous work using microprisms has been done chronically for up to 60 days (45, 46, 49), with minimal tissue inflammation (44). The current study was initially done on anesthetized animals to examine and validate the new approach, which later revealed similar organizational differences between LC and DC in awake animals. Although imaging through a microprism and 1-mm cover glass appears to have minimal impact on image quality compared to direct 2P imaging (50), it was important to compare LC imaging via microprism with the direct 2P imaging of the dorsal surface to validate the new imaging method. We found no significant differences between LC response properties when imaging via microprism or imaging directly from the dorsal surface. However, we did observe significant functional differences between the LC and the DC.

Responsiveness to spectral and temporal features.

While the LC showed inconsistent and fragmented tonotopy, the DC showed a consistent one, which was reported before (12, 13). However, the surface of the DC was biased to lower frequencies than the DC, which is consistent with previous imaging and recording studies (24, 29-31). Despite their response to pure tones, the DC and LC, particularly in the matrix, were more responsive to AM-noise, which fits their function as nonlemniscal divisions (6, 51, 52). Consistently, some recorded units in the LC was found to have higher firing rate to broadband noise than to their characteristic frequency (53). Given its critical role in communication for humans and animals (32-34, 37), the IC neurons demonstrate tuned rate responses to temporally-patterned stimuli across different species (33, 35, 54, 55). To our best knowledge, all of the work studying the temporal coding of the IC was run through recording electrodes spanning the dorsoventral axis of the IC targeting mostly the central nucleus. However, recoding

390 from the superficial portion of such a dorsoventral axis revealed the presence of unsynchronized
391 neurons to the AM-noise, which is likely located on the DC (36).

392 The spectral and temporal features of animal vocalization and speech are not independent (34).
393 We observed that neurons in the LC, particularly in the matrix, had greater responsiveness to
394 spectral and temporal modulation than neurons in the DC. Given the role of inhibition in the
395 spectral and temporal processing (56-58), the GABAergic cells of the modules could play an
396 important role to increase the spectral and temporal modulation indices, especially at lower
397 sound levels, which could be critical for localizing objects in noisy environments given the
398 importance of spectral and temporal cues for sound localization (59-61). Therefore, future work
399 is critical to image the functional responses of the GABAergic cells of the modules and compare
400 them with the non-GABAergic cells inside and outside the modules.

401 *Somatosensory vs. auditory response:*

402 In the LC, we observed that most auditory-responsive neurons, particularly onset-responsive
403 neurons, were found in the matrix, which receives mostly auditory inputs (17). However, a
404 subpopulation of acoustically-driven offset-responsive neurons preferably resides in the
405 modules compared to the matrix. Given that the offset response could be generated as a
406 rebound to the termination of the ongoing inhibition during the sound presentation (62),
407 GABAergic cells in the modules could play an important role in the coding of sound termination
408 as found before in the cortex (63). Because some of the offset acoustically-driven cells inside
409 the modules were also activated by the somatosensory stimulation, this fraction of cells could
410 then encode the termination of somatosensory-associated sounds through the local inhibitory
411 circuits of the modules. Under in-vivo recording of the mouse IC, the offset responses were
412 previously reported from cells that were non-GABAergic and preferably located in the caudal
413 and shallower parts of the IC (64).

Consistent with the previous reports, we observed that combined auditory-somatosensory stimulation generally suppressed neural responses to auditory stimuli when presented alone and that this suppression was most prominent in the LC matrix. These findings are consistent with other reports demonstrating auditory-somatosensory suppression in the nonlemniscal IC (20, 42). Mechanistically, it is not known if such suppressive responses are created in the LC or are inherited from other brain regions since auditory-somatosensory interactions occur as early in the cochlear nucleus, and are also found in the IC, thalamus, and cortex (65-72), reviewed in (41, 73). We note that a systematic exploration of the stimulus space was not conducted here such that other acoustic or somatosensory stimuli, different relative amplitudes, or different relative timings of the stimuli could have produced enhancement rather than suppression. Future work will be needed to further explore this stimulus space to more fully understand multisensory processing in the LC.

Conclusions:

Here, using a novel microprism approach to image the LC in anesthetized and awake mice, we observed that 1) DC displayed tonotopic organization which was not consistently present in the LC, 2) DC neurons were generally more sound-responsive than LC neurons but that neurons in both regions had preferential responses to spectrally- and temporally-complex stimuli, 3) that matrix regions of the LC were more responsive to spectrally- and temporally-complex stimuli than modules and that modules were more responsive to somatosensory stimuli and 4) that bimodal stimulation led to suppressive responses that were more prominent in the matrix and enhancement that was more prominent in modules. These data highlight significant organizational differences between the LC and DC and between modules and matrix in the LC. Future work using microprisms in the LC will help to reveal the potential differential role of matrix vs. module neurons in multisensory integration tasks in behaving animals.

Materials and methods:

439 **Animal subjects:**

440 Male mice of 8-12 weeks of age were used. Males were used as our preliminary data suggest
441 male/female differences in DC organization (74) and will be published separately. GAD67-GFP
442 knock-in mice (developed and shared with permission from Dr. Yuchio Yanagawa at Gunma
443 University and obtained from Dr. Douglas Oliver at the University of Connecticut), where GFP is
444 exclusively expressed in GABAergic cells (25), were used to visualize the GABAergic cells and
445 LC modules. To simultaneously monitor calcium signals and visualize the GFP+ cells, Tg(Thy1-
446 jRGECO1a)GP8.20Dkim/J mice (Jackson Laboratory, Stock# 030525) were crossed with
447 GAD67-GFP knock-in mice to generate GAD67-GFPxThy1-jRGECO1a hybrid mice. The mice
448 were housed and bred at the animal research facility of The Beckman Institute for Advanced
449 Science and Technology. The animal care facilities are approved by the Association for
450 Assessment and Accreditation of Laboratory Animal Care (AAALAC). To phenotype the GFP-
451 positive animals, an epifluorescence microscope was used for the transcranial examination of
452 the pups at postnatal day 4 using excitation: 472/30 nm and emission 520/35 nm filters along
453 with dichroic 505 nm long pass at low power magnification (2.5x/0.08, Olympus objective,
454 MPlanFL N, Japan). The positive pups exhibited a green fluorescence in the cerebellum, the
455 cerebral cortex, and the olfactory bulb and were only kept with their parents until weaning. The
456 genotyping for jRGECO1a was done using a probe composed of a forward primer:
457 GCCGCCGAGGTCAAGA & a reverse primer: TCCAACTTGATGTCGACGATGTAG) by
458 Transnetyx™ (Transnetyx, USA). Samples of the mice's tail snip around one month of age were
459 used for genotyping. All applicable guidelines for the care and use of animals were followed. All
460 procedures were approved by the Institutional Animal Care and Use Committee (IACUC).

461 **Surgery**

462 The general procedures of craniotomy were previously described (27), with modifications to
463 place craniotomy over the IC. Before surgery, mice were anesthetized with a mixture of

464 ketamine, xylazine, and acepromazine (100 mg/kg, 3 mg/kg, and 3mg/kg, respectively)
465 delivered intraperitoneally. The anesthesia was maintained during the surgery and imaging
466 using only ketamine (100 mg/kg). To prevent neural edema during or after the craniotomy, an
467 intramuscular injection of dexamethasone sodium (4.8 mg/kg) was given just before the surgery
468 using an insulin syringe. After placing the animal in the stereotaxic apparatus (David Kopf
469 Instruments, USA), both eyes were protected by applying Optixcare lubricant eye gel (Aventix
470 Animal Health, Canada). The hair on the scalp was then removed by massaging the scalp with
471 a depilatory cream (Nair) using a cotton-tipped applicator and leaving the cream on the scalp for
472 4-5 minutes. The cream was then removed by a thin plastic sheet (flexible ruler) to leave a hair-
473 free area on the scalp**.** The remaining tiny hairs were then removed by alcohol swab and the
474 area was then sterilized by applying 10% Povidone Iodine (Dynarex, USA) using a sterile
475 cotton-tipped applicator. The medial incision was made with a scalpel blade #10, and 0.2 ml of
476 0.5% lidocaine was injected intradermally into the scalp. The skin extending from the medial line
477 to the temporalis muscle was completely removed using a pair of microscissors to produce a
478 wide skinless area above the skull. A pair of no. 5/45 forceps were used to remove any
479 remaining periosteum. The remaining dried or firmly attached pieces of periosteum were
480 removed with a scalpel blade #10. The skull was cleaned with sterile saline and dried with
481 gently pressurized air. Using the stereotaxic apparatus, a wide area of ~3 x 4 mm above the left
482 IC was made. A micro drill bit (size #80, Grainger, USA) was used to drill through the skull
483 starting from the rostrolateral (Figure 1A, yellow circle) region to lambda (Figure 1A, black circle)
484 following the border in a clockwise direction (Figure 1A, dotted black rectangle). To prevent
485 overheating of the superficial brain tissues and to mitigate the occasional spurts of skull
486 bleeding during the drilling, ice-cold sterile saline was used to intermittently irrigate the surface.
487 A stream of pressurized air was also applied during the drilling procedures to prevent
488 overheating and remove the debris produced by the drilling. Caution was taken not to pierce the
489 dura when performing the craniotomy while crossing the sagittal or the lambdoid sutures to

490 avoid damaging the underlying sinuses. After drilling, the skull was irrigated in sterile saline and
491 the bone flap (the undrilled bone over the craniotomy area) was gently examined for complete
492 separation from the rest of the skull (Figure 1B). Using a pair of no. 5/45 forceps, the bone flap
493 was gently removed. To control the bleeding if it occurred, a piece of sterile hemostatic gel
494 (Adsorbable Gelatin Sponge USP, Haemosponge, GBI, India) which was pre-soaked in ice-cold
495 saline, was applied to the bleeding spot. Once the bleeding ceased, the brain was kept covered
496 in sterile saline. In some surgeries, the dura was peeled off from the surface of the IC while
497 removing the bone flap. In the surgeries where the dura remained intact, a Bonn microprobe
498 (F.S.T, Germany, Item # 10032-13) was used to pierce the dura in an area that is not above the
499 IC and devoid of cortical vasculature (e.g., a part of exposed cerebellum). After piercing, the
500 dura was carefully and gently lifted, and a pair of no. 5/45 forceps were used to grab the dura to
501 gently tear it to the extent of the transverse sinus to avoid bleeding of the major venous
502 structures.

503 Using the stereotaxic apparatus, a 30° diamond knife (F.S.T, Germany, Item # 10100-30) was
504 placed in its vertical position. From the medial line, the knife was placed at the lateral horizon of
505 the IC. The knife was then inserted 1.5 mm ventrally. Caution was taken to avoid hitting any
506 major blood vessels to avoid bleeding. From its position, the knife was retracted 0.3-0.5 mm
507 medially to create an initial pocket for the insertion of the microprism (Figures 1C-E). The
508 microprism (1.5 mm-silver coated, Tower Optical Corporation) was then inserted, so one of its
509 sides was parallel to the lateral surface of the diamond blade, the other side was facing up, and
510 its hypotenuse was facing ventrally (Figures 1F and G). The wooden piece of a cotton swab was
511 carefully driven down to push the microprism until its top surface was at the same level as the
512 IC dorsal surface. Keeping the microprism in its place with the wooden end of a swab, the
513 diamond knife was carefully retracted upward leaving the microprism behind (Figure 1H). If the
514 retraction of the diamond knife pulled the prism up, the wooden piece would be used to push it

515 down simultaneously with the knife movement. To control the bleeding, a piece of sterile
516 hemostatic gel was used as before. The tip of the diamond knife was used to secure the
517 microprism in its position for at least 10 minutes (Figures 1I and J). During that time, the solution
518 of the 1% agarose was prepared for use. A pair of forceps were then used to gently place a
519 sterile 5 mm cover glass #1 (Thomas Scientific, USA) over the skull covering the opened area
520 above the IC. The cover glass was secured by a wooden trimmed piece of sterile cotton swab
521 by gently pressing the cover glass from the top. Since the surface of the IC was located below
522 the surfaces of both the cerebellum and cerebral cortex, the cover glass usually traps about a
523 0.7-1.0 mm thick sheet of sterile saline. The movement of the liquid medium caused by heart
524 pulsation was found to be a source of motion artifact during imaging, so the gap between the
525 surface of the IC and the cover glass was filled with 1% agarose gel that was made in saline at
526 a temperature range of 33-35°C (Figure 1K). The extra agarose gel pieces were cut off and
527 removed by the scalpel blade and the wet skull was then dried out using pressurized air. A
528 titanium headpost as described before (27) was glued carefully on the top of the skull to be at
529 the same level as the cover glass. Following the manufacturer's instructions, the C&B Metabond
530 (Parkell, Japan) was used to secure the headpost in its place. Excluding the steps of the
531 microprism insertion, the same procedures were followed for DC imaging from the surface
532 (Figure 1L). For awake preparations, the same procedures were followed under isoflurane
533 anesthesia starting with 4% of isoflurane as an induction dose with 1-2% isoflurane during the
534 surgery. The animal was transferred under the microscope objective and left to recover from
535 isoflurane anesthesia for 1 hour before imaging. To ensure the animal's recovery, the animal
536 was visually inspected for its breathing rate (75) and for ongoing limb movements.

537 **Acoustic stimulation:**

538 Using a custom-made MATLAB (The MathWorks, Natick, MA, USA) code, either 500 ms pure
539 tone or AM-noise was generated. Thirty-five (5x7) pure tones with a series of sound pressure

levels (40, 50, 60, 70, 80 dB SPL) and a series of carrier frequencies (5000-40000 Hz with a half-octave gap) were presented with a cosine window. Forty-five (5x9) 100% AM white noise bursts with a series of sound pressure levels (40, 50, 60, 70, 80 dB SPL) and modulation frequencies (0, 2, 4, 8, 16, 32, 64, 128, 256 Hz) were generated. The stimuli of either pure tone or AM-noise combinations were played in random sequence to the mice with a 600 ms interstimulus interval (ISI) by a TDT RP2.1 processor (Tucker-Davis Technologies, US) and delivered by a TDT ES1 speaker (Tucker-Davis Technologies, US). In other sets of experiments, 500 ms of nonmodulated broadband noise was presented 5 times with ISI of 600 ms at 80 dB SPL to examine the acoustic activity between modules and matrix compared to somatosensory stimulation.

The output of the TDT ES1 speaker was calibrated using a PCB 377A06 microphone, which feeds a SigCal tool to generate a calibration file for all tested frequencies (5–40 kHz). To enable the custom-made MATLAB code to read this calibration file, the values were first processed by MATLAB signal processing toolbox (sptool) to generate a 256-tap FIR filter to apply the calibration using the following parameters [arbitrary magnitudes, least square, order: 256, sampling rate: 97,656.25, frequency vector (5–40 kHz), amplitude vector (40–80 dB SPL), and weight vector ones (1128)].

Somatosensory stimulation:

The somatosensory stimulation was done by deflecting the right whiskers of the animals at an average excursion of 1.2 mm with a 50 Hz rate over 500 ms to match the acoustic stimulus. A total of five stimuli were presented with 600 ms ISI. The whisker deflection was performed using a Brüel & Kjær vibrator (V203 10/32 UNF- CE, United Kingdom) that was driven by a wave generator (4063, BK precision, USA) after amplifying the signals with an SLA1 100 W power amplifier (ART, USA).

564 **Two-Photon imaging:**

565 Immediately after surgery, the anesthetized animal was taken and secured under the
566 microscope objective by clamping the arms of the head post to two perpendicular metal posts
567 mounted on the microscope stage. A custom-built 2P microscope was used. The optical and the
568 controlling components were supplied from Bruker, Olympus, and Thorlabs. The imaging of the
569 DC was made using a 20X water-immersion objective (LUMPlanFI/IR, 20X, NA: 0.95, WD: 2
570 mm; Olympus Corporation, Tokyo, Japan), while the lateral surface of the IC was imaged by the
571 long working distance 16x water-immersion objective (N16XLWD-PF - CFI LWD Plan Fluorite
572 Objective, 16X, NA: 0.8, WD: 3.0 mm; Nikon, Tokyo, Japan) to be able to reach the focal point
573 of the microprism at its hypotenuse. For imaging both the GFP or jRGECO1a signals, the
574 excitation light was generated by InSight X3 laser (Spectra-Physics Lasers, Mountain View, CA,
575 USA) tuned to a wavelength of 920 or 1040 nm, respectively. A layer of a 1:1 mixture of
576 wavelength multipurpose ultrasound gel (National Therapy, Canada) with double deionized
577 water was used to immerse the objective. This gel was able to trap the water and reduce its
578 evaporation during imaging. The emitted signals were detected by a photomultiplier tube
579 (Hamamatsu H7422PA-4, Japan) following a t565lp dichroic and a Chroma barrier et525/70m
580 filter for GFP and et595/50m filter for jRGECO1a signals. Images (512x512 pixels) were
581 collected at a frame rate of 29.9 Hz in the resonant galvo mode. Data were collected from the
582 dorsal surface of the IC by scanning the surface of the IC based on the GFP and jRGECO1a
583 signals through the medial and lateral horizons of the IC. Generally, the scanning was started by
584 moving the 20x objective to the most ventromedial position, where there is no ability to see any
585 cells (Figure 2B, medial horizon). Then, the objective was started to slowly move dorsolaterally
586 to get cells in focus (Figure 1M), where the average depth of the first field of view was 169 μm.
587 The lateral movement of the objective was intended to be aligned and parallel to the curvature
588 of the DC surface indicated by getting the superficial cells in focus to avoid any possibility of

589 imaging the upper layers of the central nucleus of the IC, so the average depth of the most
590 superficial point of the imaging was 92 μm. The scanning was ended by moving the objective to
591 the most ventrolateral position of the IC, where there is no ability to see GFP laterally (Figure
592 2B, lateral horizon), where the last field of view was collected at an average depth of 225 μm.
593 Generally, each field of view was selected based on the expression of GFP signals as an
594 indicator for the cells in focus and being acoustically active by using a search stimulus that was
595 500 ms broadband noise with zero modulation at 80 dB SPL. The z-axis of the objective was
596 determined relative to the pia surface. The relative position of each region was tracked through
597 the micromanipulator (MP-285, Sutter Instruments) that controlled the microscope objective.
598 The positions of imaged areas were further aligned across animals to a common coordinate
599 using the midline, lateral extremes, and the vasculature landmarks taken via imaging of the GFP
600 signals of the cranial window with low magnification (4x Olympus objective, 4x4 binning, 50 ms
601 frame time) using a Lumen 200 bulb (Prior Scientific Inc, USA) and CoolSNAP MYO camera
602 (Photometrics, USA, excitation: 488 nm and emission: 515–550 nm). Imaging of the lateral
603 surface of the IC via microprism was done similarly. However, a 16x objective with a long
604 working distance was used to enable reaching the focal point at the microprism hypotenuse. In
605 both cases, the frame timing of the scanner and the sound stimuli were both digitized and time-
606 locked using a Digidata 1440A (Molecular Devices, Sunnyvale, CA, USA) with Clampex v. 10.3
607 (Molecular Devices, Sunnyvale, CA, USA).

608 **Laser lesion:**

609 The laser lesion was produced using a 720 or 820 nm laser beam at 74-80 mW power at the
610 level of the objective for 100 to 250 seconds depending on the size of the lesioned area, the
611 speed of laser scanning (frame rate), and the depth of the lesion (z-axis length). In brief, the
612 area of interest and the dimension of the laser lesion were initially determined using 920 nm as
613 indicated by the GFP signals through scanning one of the GABAergic modules. The depth of the

614 GABAergic modules was then determined by counting the optical slices starting from their
615 superficial surface. The tunable laser was then switched from 920 nm to the shorter wavelength
616 (720 or 820 nm) to scan the same area and depth at a rate (1-2 frames/ second).

617 **Data processing:**

618 *Data collection:* The data were collected as separate movies (512x512 pixels) for each pure
619 tone or AM-noise runs in a resonant galvo mode. Depending on the amplitude and frequency
620 combinations for each type of acoustic stimulus, 40- or 52-second periods were assigned as a
621 movie's length for pure tone (35 stimulus combinations), or AM-noise (45 stimulus
622 combinations), respectively. Using ImageJ software, the z-projection was used to compute one
623 single image representing either the sum, the standard deviation, or the median of all the image
624 sequences in the movie. Based on these single images, the region of interest (ROI) was
625 manually drawn around each detectable cell body. Figures 4A and B represent the sum of the
626 images sequences of the movie collected from the dorsal surface, or the lateral surface of the IC
627 via microprism, respectively. For the subsequent processing steps, Python open-source libraries
628 were used (listed below).

629 *Motion Correction and Filtering:* The imread function from the OpenCV library was used in
630 grayscale mode to import images into a numpy array from a single folder containing TIFF
631 images. The array was then exported as a single TIFF stack into a temporary folder using the
632 mimwrite function from the imageio library, and the process was repeated for each folder. The
633 NoRMCorre algorithm (76) embedded in the CaImAn library (77) was used to apply motion
634 correction to each of the TIFF files. The data were then imported into a numpy array, rounded,
635 and converted to 16-bit integers. The images were filtered using a 2D Gaussian filter with a
636 sigma value of 1 (surface View) / 2 (prism View) in each direction, then a 1D Gaussian temporal
637 filter with a sigma value of 2 was applied using the ndimage.gaussian_filter and
638 ndimage.gaussian_filter1d function from the scipy library, respectively.

Data Extraction: The ROI sets, which were manually created using ImageJ, were imported using the read_roi_zip function from the read_roi library. The sets were then used to create two masks; one mask was used as a replica of the ROIs and the second mask was made around the original ROI (roughly four times larger in area). The smaller mask was applied to find the average pixel value within each ROI, while the larger mask was applied to find the average pixel value of the neuropil. The neuropil correction was applied using the following equation (78);

$$\text{Corrected value} = \text{Date value} - (0.4 \text{ X Neuropil value})$$

To identify the calcium signals, Δf/f was calculated by using the following equation.

$$\frac{\Delta \mathrm{f}}{\mathrm{f}} = \frac{(\text{Date value} - \text{Background value})}{\text{Background value}}$$

where the background value is the slope estimating the background levels with fluorescence bleaching factored in. The data were then reorganized so that all segments with the same stimulus frequency and stimulus amplitude were grouped. The area under the curve (AUC) of the calcium signals was then used as a metric to determine the magnitude of the response and for subsequent analysis (79, 80).

Cell Flagging: The correlation coefficient between each of the trials was calculated using the stats. Pearson function from the scipy library. The average correlation coefficient was calculated for each stimulus frequency and stimulus amplitude. Similar to previous work (12), if the average correlation coefficient was above the threshold of 0.6, the cell was flagged as being responsive to that stimulus combination of frequency and amplitude, and the best tone and modulation frequencies were calculated for every cell (13). Knowing the best tonal frequency (BTF) and modulation frequency (BMF) for each neuron enabled us to calculate the SMI and TMI following these equations;

SMI

$$= \frac{\text{Response to BTF} - \text{Response to unmodulated noise}}{\text{Response to BTF} + \text{Response to unmodulated noise}}$$

The SMI has values ranging from (-1 to 1). While neurons with values closer to 1 are more responsive to pure tone, neurons with values closer to -1 are more responsive to noise with no modulation.

$$\text{TMI} = \frac{\text{Response to BMF} - \text{Response to unmodulated noise}}{\text{Response of BMF} + \text{Response to unmodulated noise}}$$

Similarly, the TMI has values ranging from (-1 to 1). While neurons with values closer to 1 are more responsive to AM-noise, neurons with values closer to -1 are more responsive to noise with no modulation.

For the comparison between somatosensory and auditory responses, the threshold of 0.4 was used as a cutoff threshold to determine the responsive cells to each stimulation. The average response of each somatosensory, acoustic (500 ms of unmodulated noise), or simultaneous somatosensory and acoustic (bimodal) stimulation was then calculated for each responsive cell.

To examine the effect of somatosensory stimulation on auditory responses, the response index (RI) was calculated for the auditory-responsive cells using the following equation;

$$\text{RI} = \frac{\text{Auditory response to bimodal stimulation}}{\text{Auditory response to auditory stimulation only}}$$

Reurons with RI values > 1 have enhanced or higher responses induced by simultaneous auditory and somatosensory stimulation, while neurons with RI values < 1 have downregulated or suppressed auditory responses induced by auditory and simultaneous somatosensory stimulation.

683 *Map Generation:* The average radius for all ROIs was calculated to ensure that all cells on the
684 tonotopic map had uniform radii. A color key was also generated for every corresponding map.
685 A blank canvas was generated using the Image module from the pillow library, and a circle was
686 created for each cell and filled with a corresponding color to its value.

687 **Statistics:**

688 All statistical analyses and graphs were made using Origin Pro 2022 software. The normality of
689 the distributions of the data was examined using a Kolmogorov-Smirnov test. The Mann-
690 Whitney test as well as two-sample or paired t-test were used to examine the difference in data
691 distribution or the difference between samples of non-normal and normal distribution,
692 respectively. Either one-way or two-way ANOVA as well as Fisher as a post hoc test were used
693 for the mean comparison between different groups of normal distribution. The Chi-square (χ^2)
694 test was used to compare the samples based on cell numbers of their cellular population. The
695 cumulative frequency function was computed to calculate the fraction of cells tuned at each
696 frequency based on their best frequency. Differences were deemed significant when p-value
697 <0.05. The upper and lower dimentians of the each box plot are at the 25th and 75th percentile,
698 with whiskers at 95% spread.

699 **Histology:**

700 After the 2P imaging, the mouse was transcardially perfused with 4% paraformaldehyde (PFA)
701 solution in PBS solution. The isolated brain was then placed overnight in PFA for a complete
702 fixation. The brain was then moved from the PFA to a graded sucrose solution (10, 20, and
703 30%) until it sunk. 50 μm coronal sections were taken at the level of the IC using a Leica
704 cryostat. The sections were then mounted on a slide, coverslipped, and imaged using an
705 epifluorescence microscope for imaging the GFP signals as an indicator for the GABAergic cells
706 in the GAD67-GFP knock-in mouse (excitation: 488 nm and emissions: 515–550 nm).

707 **Artwork:**

708 The cartoon of the mouse brain in Figures 1 C, F, and I was obtained from Brain Explorer 3D
709 viewer Allen Mouse Brain (https://connectivity.brain-map.org/3d-viewer?v=1) and modified to be
710 suitable for illustration. All figures were designed and made using Adobe Illustrator (Adobe, San
711 Jose, CA). To keep working within the Adobe environment to avoid losing the resolution of the
712 figures, Adobe Photoshop (Adobe, San Jose, CA) was used to crop the borders of some images
713 to save space.

714 **Acknowledgment**

715 We thank Dr. Kush Paul (Bruker) for initial training on the craniotomy surgery, Dr. Jason
716 Maclean (The Department of Neurobiology, University of Chicago) for assistance with 2P
717 imaging, Dr. Michael Jacobs Goard (Neuroscience Research Institute, The University of
718 California- Santa Barbara) for his guidance in the use of microprisms, Dr. Taher Saif
719 (Department of Mechanical Science and Engineering, The University of Illinois Urbana-
720 Champaign) for measuring the deflecting distance of the somatosensory stimulating probe using
721 a high-speed camera. We also thank the NIDCD for funding this work under grant #
722 R01DC013073 and R01DC016599.

723 **Competing interests**

724 On behalf of all authors, there are no financial or non-financial competing interests to be
725 declared.

726 **References**

727 1. Ito T, Oliver DL. The basic circuit of the IC: tectothalamic neurons with different patterns of
728 synaptic organization send different messages to the thalamus. Front Neural Circuits. 2012;6:48.
729 2. Willard FH, DK R. Anatomy of the central auditory system. In: JF W, editor. The auditory
730 psychobiology of the mouse. Springfield, IL: Thomas; 1983. p. 201-304.
731 3. JF W. Handbook of mouse auditory research. In: JF W, editor. Behavior to molecular biology.
732 Boca Raton, FL: CRC; 2001.

4. DL O. Neuronal organization in the inferior colliculus. In: JA W, CE S, editors. The inferior colliculus. New York: Springer; 2005. p. 69–114.
5. Schreiner CE, Winer JA. The inferior colliculus: Springer Science+ Business Media, Incorporated; 2005.
6. Loftus WC, Malmierca MS, Bishop DC, Oliver DL. The cytoarchitecture of the inferior colliculus revisited: a common organization of the lateral cortex in rat and cat. Neuroscience. 2008;154(1):196-205.
7. Saldaña E, Feliciano M, Mugnaini E. Distribution of descending projections from primary auditory neocortex to inferior colliculus mimics the topography of intracollicular projections. J Comp Neurol. 1996;371(1):15-40.
8. Winer JA, Larue DT, Diehl JJ, Hefti BJ. Auditory cortical projections to the cat inferior colliculus. J Comp Neurol. 1998;400(2):147-74.
9. Bajo VM, Moore DR. Descending projections from the auditory cortex to the inferior colliculus in the gerbil, Meriones unguiculatus. J Comp Neurol. 2005;486(2):101-16.
10. Coleman JR, Clerici WJ. Sources of projections to subdivisions of the inferior colliculus in the rat. J Comp Neurol. 1987;262(2):215-26.
11. Lesicko AMH, Geffen MN. Diverse functions of the auditory cortico-collicular pathway. Hear Res. 2022;425:108488.
12. Wong AB, Borst JGG. Tonotopic and non-auditory organization of the mouse dorsal inferior colliculus revealed by two-photon imaging. Elife. 2019;8.
13. Barnstedt O, Keating P, Weissenberger Y, King AJ, Dahmen JC. Functional Microarchitecture of the Mouse Dorsal Inferior Colliculus Revealed through In Vivo Two-Photon Calcium Imaging. J Neurosci. 2015;35(31):10927-39.
14. Chernock ML, Larue DT, Winer JA. A periodic network of neurochemical modules in the inferior colliculus. Hear Res. 2004;188(1-2):12-20.
15. Dillingham CH, Gay SM, Behrooz R, Gabriele ML. Modular-extramodular organization in developing multisensory shell regions of the mouse inferior colliculus. J Comp Neurol. 2017;525(17):3742-56.
16. Lamb-Echegaray ID, Noftz WA, Stinson JPC, Gabriele ML. Shaping of discrete auditory inputs to extramodular zones of the lateral cortex of the inferior colliculus. Brain Struct Funct. 2019;224(9):3353-71.
17. Lesicko AM, Hristova TS, Maigler KC, Llano DA. Connectional Modularity of Top-Down and Bottom-Up Multimodal Inputs to the Lateral Cortex of the Mouse Inferior Colliculus. J Neurosci. 2016;36(43):11037-50.
18. Lesicko AMH, Sons SK, Llano DA. Circuit Mechanisms Underlying the Segregation and Integration of Parallel Processing Streams in the Inferior Colliculus. J Neurosci. 2020;40(33):6328-44.
19. Zhou J, Shore S. Convergence of spinal trigeminal and cochlear nucleus projections in the inferior colliculus of the guinea pig. J Comp Neurol. 2006;495(1):100-12.
20. Jain R, Shore S. External inferior colliculus integrates trigeminal and acoustic information: unit responses to trigeminal nucleus and acoustic stimulation in the guinea pig. Neurosci Lett. 2006;395(1):71-5.
21. Bandyopadhyay S, Shamma SA, Kanold PO. Dichotomy of functional organization in the mouse auditory cortex. Nat Neurosci. 2010;13(3):361-8.
22. Rothschild G, Nelken I, Mizrahi A. Functional organization and population dynamics in the mouse primary auditory cortex. Nat Neurosci. 2010;13(3):353-60.
23. Romero S, Hight AE, Clayton KK, Resnik J, Williamson RS, Hancock KE, et al. Cellular and Widefield Imaging of Sound Frequency Organization in Primary and Higher Order Fields of the Mouse Auditory Cortex. Cereb Cortex. 2020;30(3):1603-22.

24. Ito T, Hirose J, Murase K, Ikeda H. Determining auditory-evoked activities from multiple cells in layer 1 of the dorsal cortex of the inferior colliculus of mice by in vivo calcium imaging. Brain Res. 2014;1590:45-55.
25. Tamamaki N, Yanagawa Y, Tomioka R, Miyazaki J, Obata K, Kaneko T. Green fluorescent protein expression and colocalization with calretinin, parvalbumin, and somatostatin in the GAD67-GFP knock-in mouse. J Comp Neurol. 2003;467(1):60-79.
26. Dana H, Novak O, Guardado-Montesino M, Fransen JW, Hu A, Borghuis BG, et al. Thy1 transgenic mice expressing the red fluorescent calcium indicator jRGECO1a for neuronal population imaging in vivo. PLoS One. 2018;13(10):e0205444.
27. Goldey GJ, Roumis DK, Glickfeld LL, Kerlin AM, Reid RC, Bonin V, et al. Removable cranial windows for long-term imaging in awake mice. Nat Protoc. 2014;9(11):2515-38.
28. Xiong B, Li A, Lou Y, Chen S, Long B, Peng J, et al. Precise Cerebral Vascular Atlas in Stereotaxic Coordinates of Whole Mouse Brain. Front Neuroanat. 2017;11:128.
29. Romand R, Ehret G. Development of tonotopy in the inferior colliculus. I. Electrophysiological mapping in house mice. Brain Res Dev Brain Res. 1990;54(2):221-34.
30. Stiebler I, Ehret G. Inferior colliculus of the house mouse. I. A quantitative study of tonotopic organization, frequency representation, and tone-threshold distribution. J Comp Neurol. 1985;238(1):65-76.
31. Shen J, Xu Z, Shen L. Topography of acoustic response characteristics in the midbrain inferior colliculus of Kunming mouse. *<i data-test="journal-ti*tle" style="margin: 0px; box-sizing: inherit;">Chinese Science Bulletin volume. 2003;48:161–5.
32. Joris PX, Schreiner CE, Rees A. Neural processing of amplitude-modulated sounds. Physiol Rev. 2004;84(2):541-77.
33. Rees A, Langner G. Temporal Coding in the Auditory Midbrain. In: Winer JA, Schreiner CE, editors. The Inferior Colliculus New York, NY.: Springer; 2005.
34. Singh NC, Theunissen FE. Modulation spectra of natural sounds and ethological theories of auditory processing. J Acoust Soc Am. 2003;114(6 Pt 1):3394-411.
35. Frisina RD. Subcortical neural coding mechanisms for auditory temporal processing. Hear Res. 2001;158(1-2):1-27.
36. Rabang CF, Parthasarathy A, Venkataraman Y, Fisher ZL, Gardner SM, Bartlett EL. A computational model of inferior colliculus responses to amplitude modulated sounds in young and aged rats. Front Neural Circuits. 2012;6:77.
37. Nelson PC, Carney LH. Neural rate and timing cues for detection and discrimination of amplitude-modulated tones in the awake rabbit inferior colliculus. J Neurophysiol. 2007;97(1):522-39.
38. Langner G. Periodicity coding in the auditory system. Hear Res. 1992;60(2):115-42.
39. Vogelstein JT, Packer AM, Machado TA, Sippy T, Babadi B, Yuste R, et al. Fast nonnegative deconvolution for spike train inference from population calcium imaging. J Neurophysiol. 2010;104(6):3691-704.
40. Yaksi E, Friedrich RW. Reconstruction of firing rate changes across neuronal populations by temporally deconvolved Ca2+ imaging. Nat Methods. 2006;3(5):377-83.
41. Lohse M, Zimmer-Harwood P, Dahmen JC, King AJ. Integration of somatosensory and motor-related information in the auditory system. Front Neurosci. 2022;16:1010211.
42. Aitkin LM, Dickhaus H, Schult W, Zimmermann M. External nucleus of inferior colliculus: auditory and spinal somatosensory afferents and their interactions. J Neurophysiol. 1978;41(4):837-47.
43. Liu M, Xie F, Dai J, Zhang J, Yuan K, Wang N. Brain-wide inputs to the non-lemniscal inferior colliculus in mice. Neurosci Lett. 2023;793:136976.
44. Andermann ML, Gilfoy NB, Goldey GJ, Sachdev RN, Wölfel M, McCormick DA, et al. Chronic cellular imaging of entire cortical columns in awake mice using microprisms. Neuron. 2013;80(4):900-13.

829 45. Low RJ, Gu Y, Tank DW. Cellular resolution optical access to brain regions in fissures: imaging
830 medial prefrontal cortex and grid cells in entorhinal cortex. Proc Natl Acad Sci U S A.
831 2014;111(52):18739-44.
832 46. Heys JG, Rangarajan KV, Dombeck DA. The functional micro-organization of grid cells revealed
833 by cellular-resolution imaging. Neuron. 2014;84(5):1079-90.
834 47. Beckmann L, Zhang X, Nadkarni NA, Cai Z, Batra A, Sullivan DP, et al. Longitudinal deep-brain
835 imaging in mouse using visible-light optical coherence tomography through chronic microprism cranial
836 window. Biomed Opt Express. 2019;10(10):5235-50.
837 48. Marks TD, Goard MJ. Stimulus-dependent representational drift in primary visual cortex. Nat
838 Commun. 2021;12(1):5169.
839 49. Wenzel M, Hamm JP, Peterka DS, Yuste R. Reliable and Elastic Propagation of Cortical Seizures
840 In Vivo. Cell Rep. 2017;19(13):2681-93.
841 50. Chia TH, Levene MJ. Microprisms for in vivo multilayer cortical imaging. J Neurophysiol.
842 2009;102(2):1310-4.
843 51. Faye-Lund H, Osen KK. Anatomy of the inferior colliculus in rat. Anat Embryol (Berl).
844 1985;171(1):1-20.
845 52. Chen C, Cheng M, Ito T, Song S. Neuronal Organization in the Inferior Colliculus Revisited with
846 Cell-Type-Dependent Monosynaptic Tracing. J Neurosci. 2018;38(13):3318-32.
847 53. Aitkin L, Tran L, Syka J. The responses of neurons in subdivisions of the inferior colliculus of cats
848 to tonal, noise and vocal stimuli. Exp Brain Res. 1994;98(1):53-64.
849 54. Rees A, Møller AR. Stimulus properties influencing the responses of inferior colliculus neurons to
850 amplitude-modulated sounds. Hear Res. 1987;27(2):129-43.
851 55. Rees A, Møller AR. Responses of neurons in the inferior colliculus of the rat to AM and FM tones.
852 Hear Res. 1983;10(3):301-30.
853 56. Wehr M, Zador AM. Balanced inhibition underlies tuning and sharpens spike timing in auditory
854 cortex. Nature. 2003;426(6965):442-6.
855 57. Cai D, Han R, Liu M, Xie F, You L, Zheng Y, et al. A Critical Role of Inhibition in Temporal
856 Processing Maturation in the Primary Auditory Cortex. Cereb Cortex. 2018;28(5):1610-24.
857 58. Chang EF, Bao S, Imaizumi K, Schreiner CE, Merzenich MM. Development of spectral and
858 temporal response selectivity in the auditory cortex. Proc Natl Acad Sci U S A. 2005;102(45):16460-5.
859 59. Sinex DG. Spectral processing and sound source determination. Int Rev Neurobiol. 2005;70:371-
860 98.
861 60. Davis KA, Ramachandran R, May BJ. Auditory processing of spectral cues for sound localization
862 in the inferior colliculus. J Assoc Res Otolaryngol. 2003;4(2):148-63.
863 61. Goodman DF, Benichoux V, Brette R. Decoding neural responses to temporal cues for sound
864 localization. Elife. 2013;2:e01312.
865 62. Xu NF, Zi-Ying Chen, Qi-Cai. The function of offset neurons in auditory information processing.
866 Translational Neuroscience. 2014;5(4):275-85.
867 63. Solyga M, Barkat TR. Emergence and function of cortical offset responses in sound termination
868 detection. Elife. 2021;10.
869 64. Kasai M, Ono M, Ohmori H. Distinct neural firing mechanisms to tonal stimuli offset in the
870 inferior colliculus of mice in vivo. Neurosci Res. 2012;73(3):224-37.
871 65. Shore SE. Multisensory integration in the dorsal cochlear nucleus: unit responses to acoustic and
872 trigeminal ganglion stimulation. Eur J Neurosci. 2005;21(12):3334-48.
873 66. Haenggeli CA, Pongstaporn T, Doucet JR, Ryugo DK. Projections from the spinal trigeminal
874 nucleus to the cochlear nucleus in the rat. J Comp Neurol. 2005;484(2):191-205.
875 67. Shore SE, Vass Z, Wys NL, Altschuler RA. Trigeminal ganglion innervates the auditory brainstem.
876 J Comp Neurol. 2000;419(3):271-85.

877 68. Lohse M, Dahmen JC, Bajo VM, King AJ. Subcortical circuits mediate communication between
878 primary sensory cortical areas in mice. Nat Commun. 2021;12(1):3916.
879 69. Aitkin LM, Kenyon CE, Philpott P. The representation of the auditory and somatosensory
880 systems in the external nucleus of the cat inferior colliculus. J Comp Neurol. 1981;196(1):25-40.
881 70. Li H, Mizuno N. Single neurons in the spinal trigeminal and dorsal column nuclei project to both
882 the cochlear nucleus and the inferior colliculus by way of axon collaterals: a fluorescent retrograde
883 double-labeling study in the rat. Neurosci Res. 1997;29(2):135-42.
884 71. Kimura A, Imbe H, Donishi T, Tamai Y. Axonal projections of single auditory neurons in the
885 thalamic reticular nucleus: implications for tonotopy-related gating function and cross-modal
886 modulation. Eur J Neurosci. 2007;26(12):3524-35.
887 72. Wong C, Chabot N, Kok MA, Lomber SG. Amplified somatosensory and visual cortical projections
888 to a core auditory area, the anterior auditory field, following early- and late-onset deafness. J Comp
889 Neurol. 2015;523(13):1925-47.
890 73. Brunelle DL, Llano DA. Role of auditory-somatosensory corticothalamic circuit integration in
891 analgesia. Cell Calcium. 2023;111:102717.
892 74. Ibrahim B, Shinagawa Y, Xiao G, Asilador A, Llano D, editors. Using Microprisms, the 2P Calcium
893 Imaging Revealed a Functional Distinction between the Dorsal & Lateral Cortices of the Mouse Inferior
894 Colliculus. Association for Research in Otolaryngology; 2022; Virtual.
895 75. Ewald AJ, Werb Z, Egeblad M. Monitoring of vital signs for long-term survival of mice under
896 anesthesia. Cold Spring Harb Protoc. 2011;2011(2):pdb.prot5563.
897 76. Pnevmatikakis EA, Giovannucci A. NoRMCorre: An online algorithm for piecewise rigid motion
898 correction of calcium imaging data. J Neurosci Methods. 2017;291:83-94.
899 77. Giovannucci A, Friedrich J, Gunn P, Kalfon J, Brown BL, Koay SA, et al. CaImAn an open source
900 tool for scalable calcium imaging data analysis. Elife. 2019;8.
901 78. Akerboom J, Chen TW, Wardill TJ, Tian L, Marvin JS, Mutlu S, et al. Optimization of a GCaMP
902 calcium indicator for neural activity imaging. J Neurosci. 2012;32(40):13819-40.
903 79. Berens P, Freeman J, Deneux T, Chenkov N, McColgan T, Speiser A, et al. Community-based
904 benchmarking improves spike rate inference from two-photon calcium imaging data. PLoS Comput Biol.
905 2018;14(5):e1006157.
906 80. Overk CR, Rockenstein E, Florio J, Cheng Q, Masliah E. Differential calcium alterations in animal
907 models of neurodegenerative disease: Reversal by FK506. Neuroscience. 2015;310:549-60.

908

909 **Figure 1: A brief Illustration of the surgical procedures.**

910 (A) A surface view of the mouse's skull showing the landmarks of the craniotomy over the IC.
911 (B) An image of the bone flap after finishing the drilling. (C-E) A cartoon and two images of the
912 brain surface showing the insertion and the pocket made by the diamond knife at the lateral
913 surface of the left IC. (F-H) A cartoon and two images of the brain surface showing the insertion
914 of the microprism into its pocket to directly face the LC after displacing the blade of the diamond
915 knife. (I-K) A cartoon and two images of the brain surface showing the final setup of the

916 microprism for two different animals. (L) An image of the brain surface showing the placement of
917 a glass window for the surface imaging of the DC. (M) A cartoon of the coronal section of the IC
918 demonstrating the different fields of views taken along the mediolateral axis parallel to the
919 curvature of the IC surface at different depths (1-5) from the pial surface. Cereb: Cerebellum,
920 Ctx: Cerebral cortex, DC: Dorsal cortex of the IC, IC: Inferior colliculus, ICC: Central nucleus of
921 the IC, Lam. Lambdoid, LC: Lateral cortex of the IC, Sag. Sagittal, SS: Sigmoid sinus, TS:
922 Transverse sinus.

923 **Figure 2: The distribution of GABAergic cells on the LC imaged via microprism, and DC**
924 **imaged from the dorsal surface.**

925 All images were taken for the GFP signals exclusively expressed in GABAergic cells. (A-B) Low
926 magnification of epifluorescent images for the GFP signals obtained from the IC surface with or
927 without the microprism, respectively. The dotted white line in B represented the medial and
928 lateral horizons of the IC. (C-E) The 2P images of the GABAergic cells on the LC imaged via
929 microprism showing the GABAergic modules across multiple animals. (D and F) The 2P images
930 of the GABAergic cells on either the dorsolateral surface of the DC imaged directly from its
931 dorsal surface showing the GABAergic modules across multiple animals (red boxes) or its
932 dorsomedial surface showing a homogenous distribution of GABAergic cells of different sizes
933 with no signs of the GABAergic modules across multiple animals (blue boxes). All solid irregular
934 white lines were made at the border of the GABAergic modules; D: Dorsal, IC: Inferior colliculus,
935 L: Lateral, R: Rostral. Cereb: Cerebellum, TS: Transverse sinus.

936 **Figure 3: The validation of imaging setup.**

937 All images were taken for the GFP signals exclusively expressed in GABAergic cells and
938 processes. (A) A low magnification image of the IC surface with the microprism showing a laser
939 lesion spot made through the microprism to validate the position of the microprism relative to the

940 IC. (B) A histological coronal section at the level of the IC showing that the laser lesion made by
941 the microprism was located at the sagittal surface of the LC imaged via microprism. (C-D) Low-
942 magnification images of the IC surface from the dorsal surface show a laser lesion spot made
943 on the dorsolateral surface of the LC on the GABAergic module. The dotted white lines
944 represent the alignment of the laser lesion to the location of the GABAergic module at the
945 dorsolateral surface. (E) A histological coronal section at the level of the IC showing that the
946 laser lesion made on the IC surface targeted the GABAergic module at the dorsolateral portion
947 of the LC. The solid irregular white line was made at the border of the GABAergic modules. D:
948 Dorsal, IC: Inferior colliculus, L: Lateral, R: Rostral, Cereb: Cerebellum, TS: Transverse sinus.

949 **Figure 4: 2P expression of jRGECO1a along with evoked signals in the DC imaged from**
950 **the dorsal surface and LC imaged via microprism.**

951 (A-B) The 2P images of the jRGECO1a expression on the DC imaged from the dorsal surface
952 and the LC imaged via a microprism, respectively. (C-D) The time traces of the evoked calcium
953 signals by either different frequencies and amplitudes of pure tones or different overall
954 amplitudes and rates of AM of broadband noise, respectively, which were obtained from two
955 different cells on the DC (top traces) or the LC imaged via microprism (bottom traces); The
956 length of the colored bars (top) indicates the intensity of the stimulus, while the color indicates
957 the tone or AM frequency depending on the color scale (bottom). AM-noise: Amplitude
958 modulated broadband noise, D: Dorsal, DC: Dorsal cortex, L: Lateral, LC: Lateral cortex,
959 m.prism: Microprism, R: Rostral.

960 **Figure 5: The auditory cellular organization of the LC imaged via microprism vs. DC**
961 **imaged from the dorsal surface.**

962 (A and C) The 2P images of GFP (green) and jRGECO1a expression (red) on either the LC
963 imaged via the microprism or the DC imaged from the dorsal surface, respectively. (B and D)

964 The pseudocolor images show the responsive cells to the pure tone of different combinations of
965 frequencies and levels on the surface of the LC imaged via the microprism or the DC imaged
966 from its dorsal surface, respectively, as well as the non-responsive cells (black filled red circles).
967 (E) The cumulative distribution function of the best tone frequencies of all cells collected either
968 from the LC imaged via microprism (blue line) or the DC imaged directly from its dorsal surface
969 (red line). D: Dorsal, L: Lateral, R: Rostral. (*$p<0.05$, LC vs. DC).

970 **Figure 6: The cellular response to pure tones and AM-noise of the LC imaged via**
971 **microprism vs. DC imaged from the dorsal surface.**

972 (A and C) Bar graphs showing the difference in the cellular response to pure tone (tone) vs. AM-
973 noise on the LC imaged via microprism or the DC imaged directly from the dorsal surface,
974 respectively (*$p<0.05$, pure tone vs. AM-noise). (B) A bar graph showing the difference in the
975 cellular response to the pure tone (tone) and AM-noise of the matrix after normalization against
976 modules imaged via microprism (*$p<0.05$, matrix vs. modules). LC: Lateral cortex, DC: Dorsal
977 cortex.

978 **Figure 7: Modulation of responses by temporal and spectral complexity in the LC imaged**
979 **via microprism vs. DC imaged from the dorsal surface.**

980 (A and B) Bar graphs showing the percentage of spectrally (two-way ANOVA: $f_{(1, 4, 9)} = 50.3$, 0.0,
981 and 4.0 - $p = 7.1\times10^{-7}$, 1.0, and 0.01 for the region, sound level, and interaction, respectively,
982 Fisher post hoc, $p = 5.1\times10^{-6}$, 4.9×10^{-4}, 0.02, 0.058, and 0.14 for modules vs. matrix at 40, 50,
983 60, 70, and 80 dB, respectively) or temporally (two-way ANOVA: $f_{(1, 4, 9)} = 19.3$, 0.0, and 1.2 - $p =$
984 7.1×10^{-7}, 1.0, and 0.32 for the region, sound level, and interaction, respectively, Fisher post hoc,
985 $p = 2.7\times10^{-7}$for modules vs. matrix) modulated cells, respectively, across different sound levels
986 in modules (green bars) vs. matrix (blue bars) imaged via microprism. (*$p<0.05$, matrix vs.
987 modules). (C and D) box plots showing the mean (black lines) and the distribution (colored dots)

988 of the SMI (two-way ANOVA: $f_{(1, 4, 14583)}$ = 48.4, 210.4, and 21.3 - $p < 0.001$ for the region, sound
989 level, and interaction, respectively, Fisher post hoc test, $p = 6.2x10^{-4}$, $4.2x10^{-5}$, <0.001, and <
990 0.001 for LC vs. DC at 40, 60, 70, and 80 dB respectively) and TMI (Figure 7D, two way
991 ANOVA: $f_{(1, 4, 16139)}$ = 431.4, 59.1, and 8.3 - $p < 0.001$ for the region, sound level, and interaction,
992 respectively, Fisher post hoc test, p = 0.002, <0.001, < 0.001, <0.001, and <0.001 for LC vs. DC
993 at 40, 50, 60, 70, and 80 dB, respectively), respectively, across different sound levels in LC
994 imaged via microprism (blue) vs. DC imaged directly from the dorsal surface (red) (*p<0.05, LC
995 vs. DC).

996 **Figure 8: The waveforms of the somatosensory vs. acoustic responses of the LC imaged**
997 **via microprism.**

998 (A-B) The time traces of the evoked calcium signals by the beginning of auditory or
999 somatosensory stimuli, respectively (onset responses). (C-D) The time traces of the evoked
1000 calcium signals by the termination of auditory or somatosensory stimuli, respectively (offset
1001 responses).

1002 **Figure 9: Types of somatosensory and auditory responses from the LC neurons imaged**
1003 **via microprism.**

1004 (A) The 2P images of GFP (green) and jRGECO1a expression (red) in the LC imaged via
1005 microprism showing the modules within white irregular lines. (B, D, and F) The pseudocolor
1006 images show the auditory or somatosensory responsive cells of the LC imaged via microprism
1007 as well as the merged response, respectively (C and E) The pseudocolor images show onset
1008 (ON), offset (OFF), or onset/offset (ON/OFF) responsive cells of the LC imaged via microprism
1009 to auditory and somatosensory stimuli, respectively. (G) The pseudocolor images show
1010 enhanced and suppressive response of the auditory responsive cells of the LC imaged via
1011 microprism following the bimodal stimulation based on their response index (RI). (H and I) Bar

1012 graphs showing the percentage of responsive cells to auditory (Aud.), somatosensory (Som.),
1013 or both stimuli in modules and matrix imaged via microprism, respectively – Modules: one-way
1014 ANOVA: $f_{(2, 11)} = 38.1$ - $p = 4.0x10^{-5}$, Fisher posthoc test, $p = 1.9x10^{-5}$ or $7.6x10^{-5}$ for the
1015 percentage of responsive cells to sound only vs. the percentage of responsive cells to
1016 somatosensory stimulation only or to both, respectively and $p = 0.23$ for the percentage of
1017 responsive cells to somatosensory stimulation only vs. both, Matrix: one-way ANOVA: $f_{(2, 11)} =$
1018 23.9 - $p = 2.4x10^{-4}$, Fisher posthoc test, $p = 1.7x10^{-4}$ or $2.4x10^{-4}$ for the percentage of responsive
1019 cells to sound only vs. the percentage of responsive cells to somatosensory stimulation only or
1020 to both, respectively - $p = 0.77$ for the percentage of responsive cells to somatosensory
1021 stimulation only vs. both) (*$p<0.05$, vs. Aud.). (J) A box plot showing the normalized cell fraction
1022 of auditory (Aud.) or somatosensory (Som.) responsive cells in the matrix normalized to those in
1023 modules imaged via microprism (*$p<0.05$, matrix vs. modules). (K) A box plot showing the cell
1024 fraction of onset (ON. Aud.) or offset (OFF. Aud.) auditory responsive cells in the matrix
1025 normalized to those in modules imaged via microprism (*$p<0.05$, matrix vs. modules). (L) A box
1026 plot showing the cell fraction of the responsive cells of enhanced (Enh. resp.) or suppressive
1027 (Supp. resp.) response in the matrix normalized to those in modules imaged via microprism
1028 following bimodal stimulation (*$p<0.05$, matrix vs. modules). D: Dorsal, R: Rostral.

1029 **Figure 10: The somatosensory vs. auditory responses over the DC neurons.**

1030 (A) A low magnification of the image obtained from the IC surface. (B-D) The top row: The 2P
1031 images of GFP (green) and jRGECO1a expression (red) of three main regions (dorsolateral,
1032 dorsal, and dorsomedial) of the DC surface imaged from the dorsal surface showing the
1033 modules within irregular white lines in the dorsolateral region, the bottom row: The pseudocolor
1034 images show the somatosensory responsive cells after somatosensory stimulations. (E) The
1035 pseudocolor images show the responsive cells of the LC imaged from the dorsal surface to
1036 merged responses of auditory and somatosensory as well as the merged responses. (F) The

1037 pseudocolor images show onset (ON), offset (OFF), or onset/offset (ON/OFF) responsive cells
1038 of the LC imaged from the dorsal surface to auditory stimulation. (G) The pseudocolor images
1039 show the enhanced and suppressive response of the auditory responsive cells of the LC imaged
1040 from the dorsal surface following the bimodal stimulation based on their response index (RI). (H)
1041 A box plot shows the percentage of somatosensory responsive cells in LC imaged either from
1042 the dorsal surface (LC (dors.)) or via microprism (LC (m. p.)) as well as the DC - one-way
1043 ANOVA: $f_{(2, 11)} = 6.7$ & $p = 0.02$, Fisher posthoc test, $p = 0.01$ or 0.01 for the percentage of
1044 somatosensory responsive cells on the DC vs. LC imaged by microprism or LC imaged from the
1045 dorsal surface, respectively - $p = 0.95$ for the percentage of somatosensory responsive cells on
1046 LC imaged via microprism vs. LC imaged from the dorsal surface) (*$p<0.05$, vs. DC). (I) A box
1047 plot showing the cell fraction of auditory (Aud.) or somatosensory (Som.) responsive cells in the
1048 matrix normalized to those in modules imaged from the dorsal surface (*$p<0.05$, matrix vs.
1049 modules). (J) A box plot showing the cell fraction of onset (ON. Aud.) or offset (OFF. Aud.)
1050 auditory responsive cells in the matrix normalized to those in modules imaged from the dorsal
1051 surface (*$p<0.05$, matrix vs. modules). (K) A box plot showing the cell fraction of the responsive
1052 cells of enhanced (Enh. Resp.) or suppressed (Supp. Resp.) responses in the matrix normalized
1053 to those in modules imaged from the dorsal surface following bimodal stimulation (*$p<0.05$,
1054 matrix vs. modules). Cereb: Cerebellum, Ctx: Cerebral cortex D: Dorsal, R: Rostral, TS:
1055 Transverse sinus.

1056 **Figure 11: The acoustic response from LC imaged via microprism and DC imaged from**
1057 **the dorsal surface in awake animals.**

1058 (A and C) The 2P images of GFP (green) and jRGECO1a expression (red) on either the LC
1059 surface imaged via the microprism or the DC imaged directly from the dorsal surface,
1060 respectively showing the modules within irregular white lines. (B and D) The pseudocolor
1061 images show the responsive cells to the pure tone of different combinations of frequencies and

1062 levels of the LC imaged via the microprism or the DC imaged directly from the dorsal surface,
1063 respectively, as well as the non-responsive cells (black filled red circles). D: Dorsal, L: Lateral,
1064 R: Rostral.

1065 **Figure 12: Unique acoustic responses from the LC imaged via microprism vs. DC imaged**
1066 **from the dorsal surface.**

1067 (A) The cumulative distribution function of the best tone frequencies of all cells collected either
1068 from the LC imaged via microprism (blue) or the DC (red). (B) A bar graph showing the
1069 percentage of responsive vs. nonresponsive cells to pure tone or AM-noise within the LC
1070 imaged via microprism or the DC (*$p<0.05$, pure tone vs. AM-noise). (C) A bar graph showing
1071 the percentage of responsive cells to pure tone or AM-noise for LC imaged via microprism vs.
1072 DC (*$p<0.05$, LC vs. DC). (D) A bar graph showing the percentage of responsive cells to pure
1073 tone or AM-noise for modules vs. matrix imaged via microprism(*$p<0.05$, matrix vs. modules).
1074 Non-resp.: Non-responsive, Resp.: Responsive.

1075 **Figure 13: The somatosensory response from LC imaged via microprism in awake**
1076 **animals.**

1077 (A, C, and E) The pseudocolor images show the auditory or somatosensory responsive cells of
1078 the LC imaged via microprism to auditory and somatosensory stimulations as well as the
1079 merged response, respectively. (B and D) The pseudocolor images show onset (ON), offset
1080 (OFF), or onset/offset (ON/OFF) responsive cells of the LC imaged via microprism to auditory
1081 and somatosensory stimulations, respectively. (F) The pseudocolor images show the enhanced
1082 or suppressed responses of the auditory responsive cells following the bimodal stimulation
1083 based on their response index (RI). (G) A bar graph showing the cell fraction of auditory (Aud.)
1084 or somatosensory (Som.) responsive cells in the matrix vs. modules imaged via microprism
1085 (*$p<0.05$, matrix vs. modules). (H) A bar graph showing the cell fraction of the responsive cells

1086 of suppressed (Supp. resp.) or enhanced (Enh. resp.) response in the matrix vs. modules

1087 imaged via microprism following bimodal stimulation (*$p<0.05$, low vs. high response). D:

1088 Dorsal, R: Rostral.

1089

Figure 1:

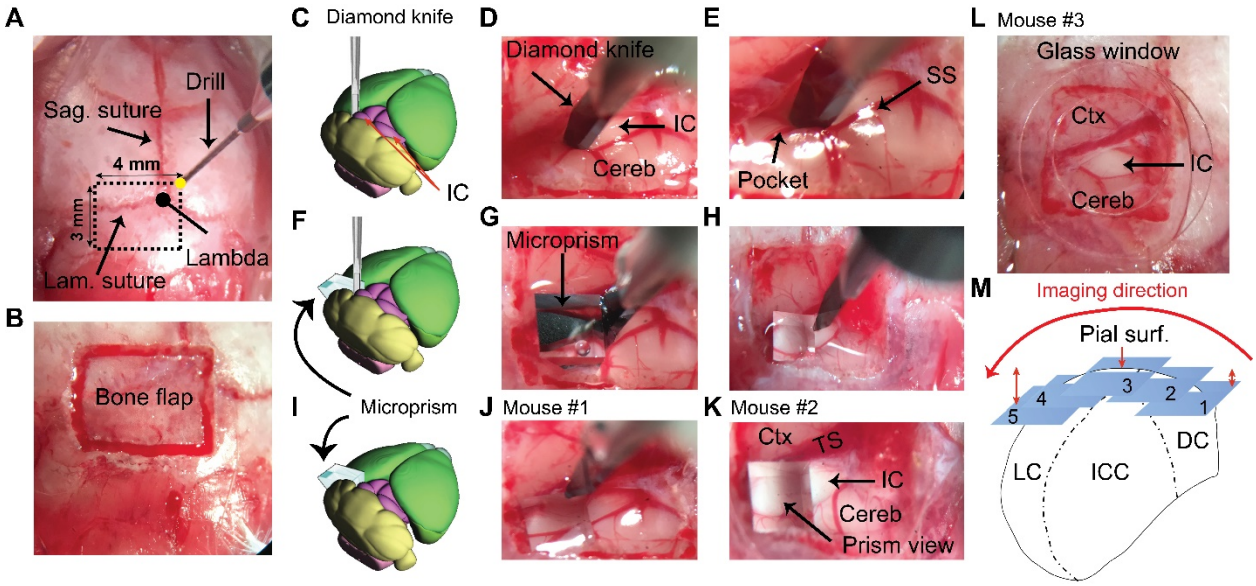
A
Drill
Sag. suture
4 mm
3 mm
Lambda
Lam. suture
B
Bone flap
C
Diamond knife
IC
D
Diamond knife
IC
Cereb
E
SS
Pocket
L
Mouse #3
Glass window
Ctx
IC
Cereb
F
G
Microprism
H
I
Microprism
J
Mouse #1
K
Mouse #2
Ctx
TS
IC
Cereb
Prism view
M
Imaging direction
Pial surf.
1
2
3
4
5
LC
ICC
DC

1093 Figure 2:

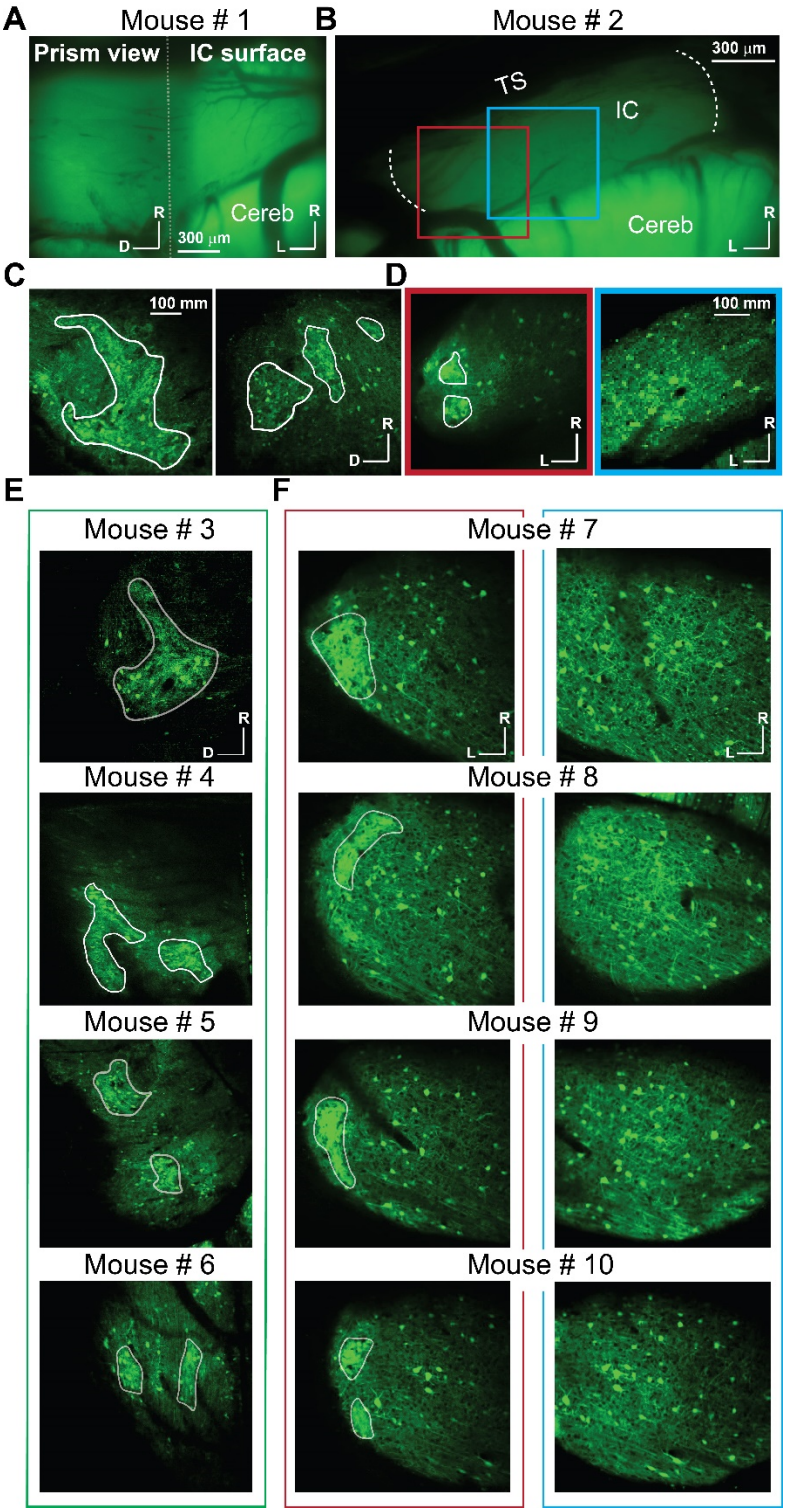

1094

1095

1096 Figure 3:

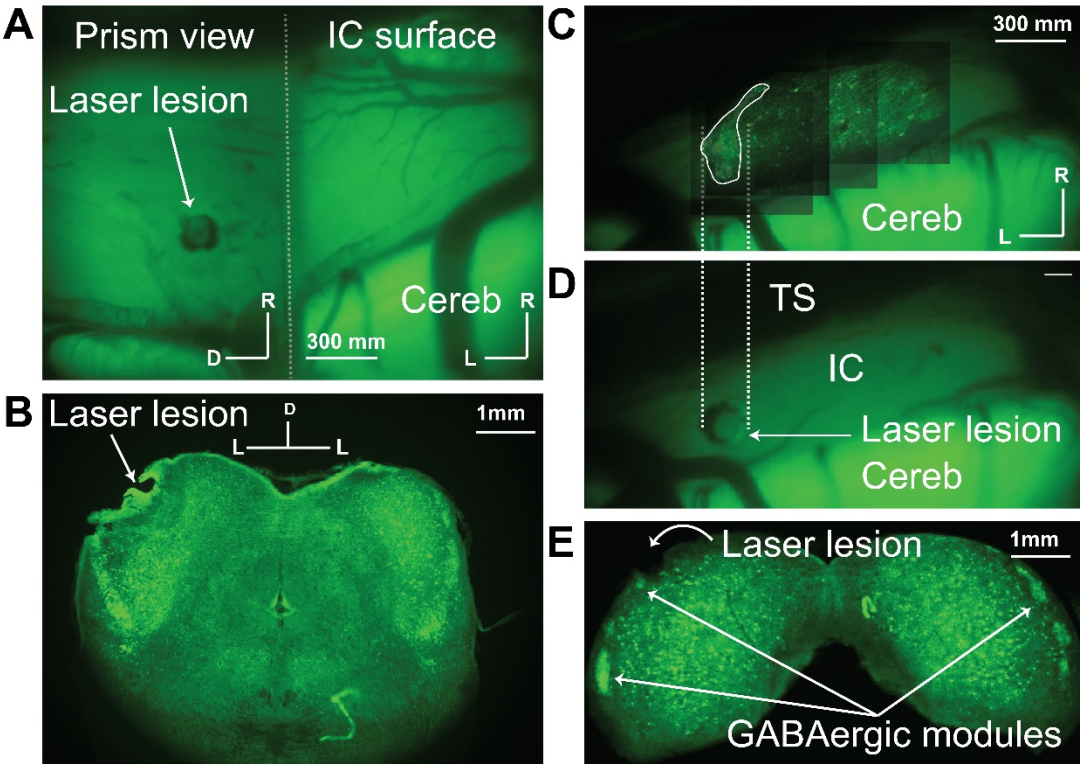

1097

1098

Figure 4:

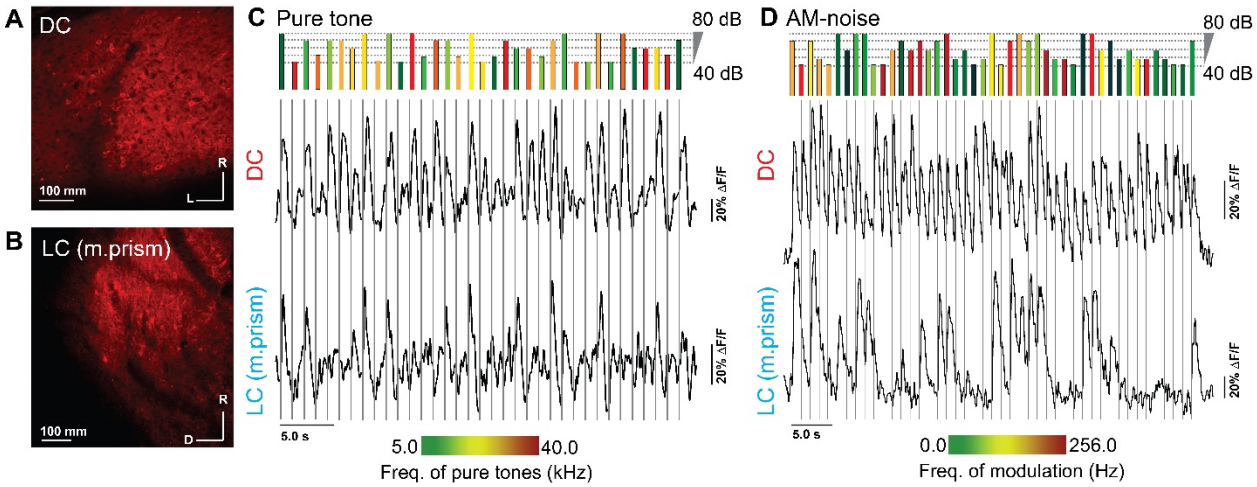
A
DC
100 mm
R
L
B
LC (m.prism)
100 mm
R
D
C
Pure tone
80 dB
40 dB
DC
LC (m.prism)
20% ΔF/F
20% ΔF/F
5.0 s
5.0
40.0
Freq. of pure tones (kHz)
D
AM-noise
80 dB
40 dB
DC
LC (m.prism)
20% ΔF/F
20% ΔF/F
5.0 s
0.0
256.0
Freq. of modulation (Hz)

Figure 5:

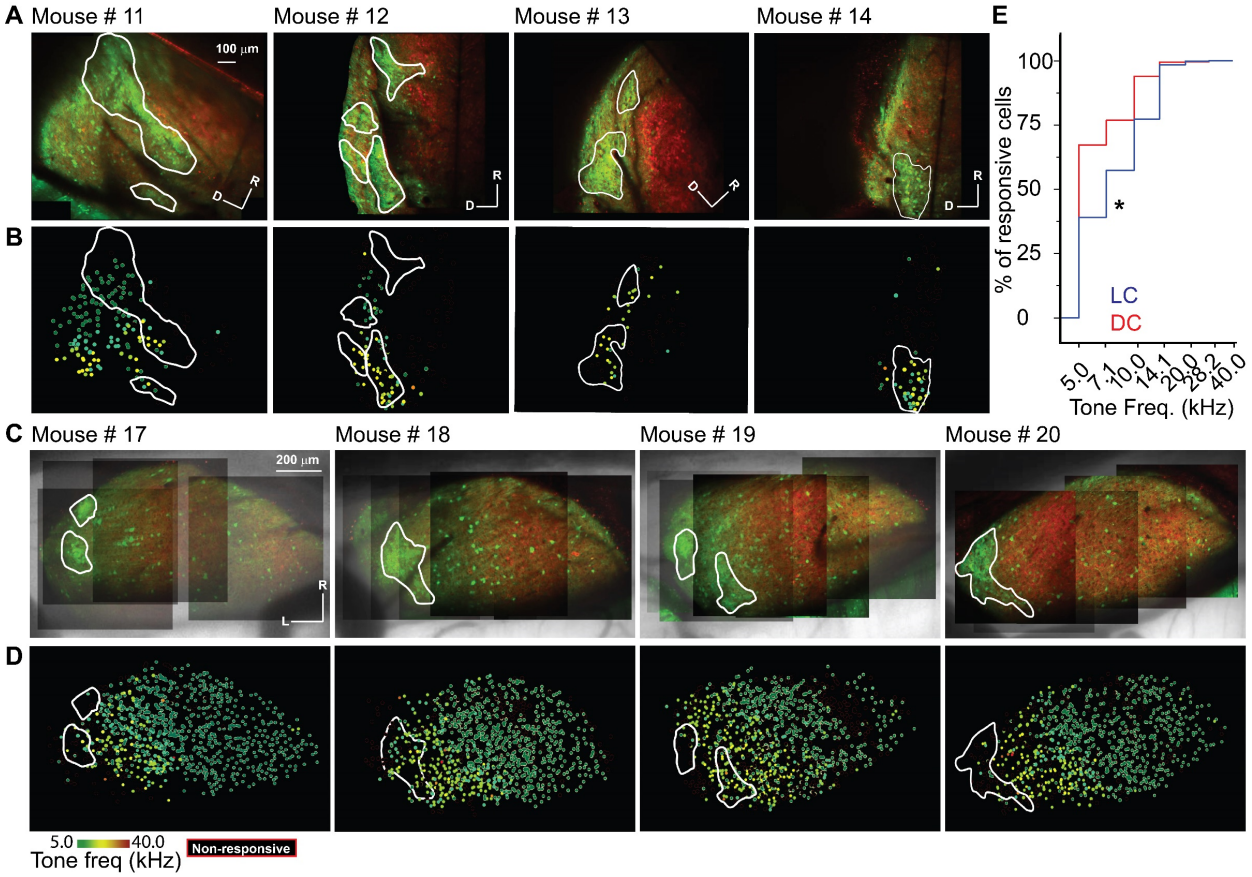
A
Mouse # 11
Mouse # 12
Mouse # 13
Mouse # 14
100 µm
R
D
B
E
100
75
50
25
0
% of responsive cells
*
LC
DC
5.0
7.1
10.0
14.1
20.0
28.2
40.0
Tone Freq. (kHz)
C
Mouse # 17
Mouse # 18
Mouse # 19
Mouse # 20
200 µm
R
L
D
5.0
40.0
Tone freq (kHz)
Non-responsive

1106 Figure 6:

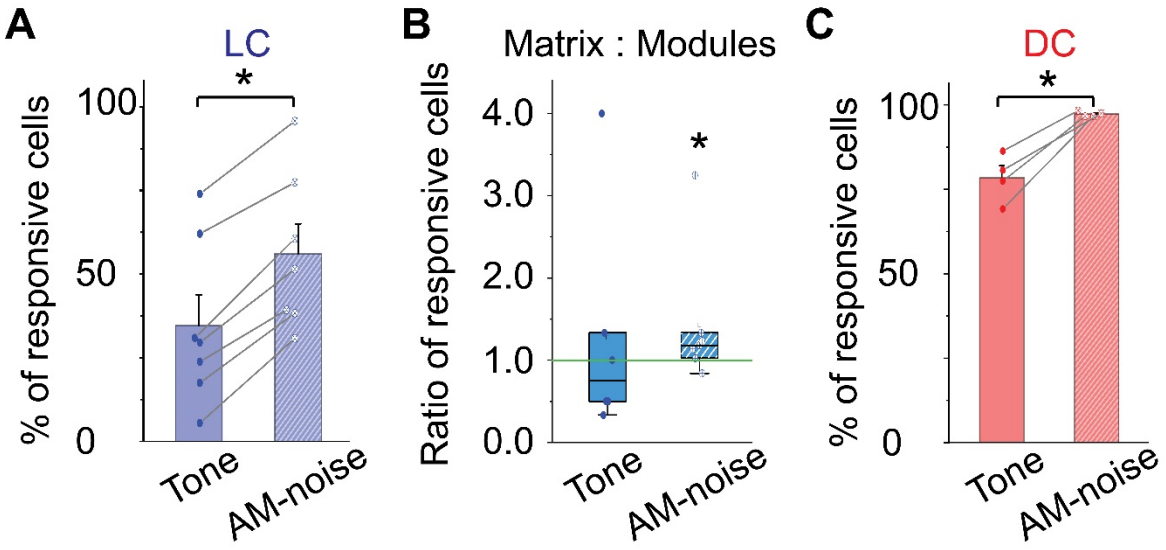

1107

1108

1109

1110 Figure 7:

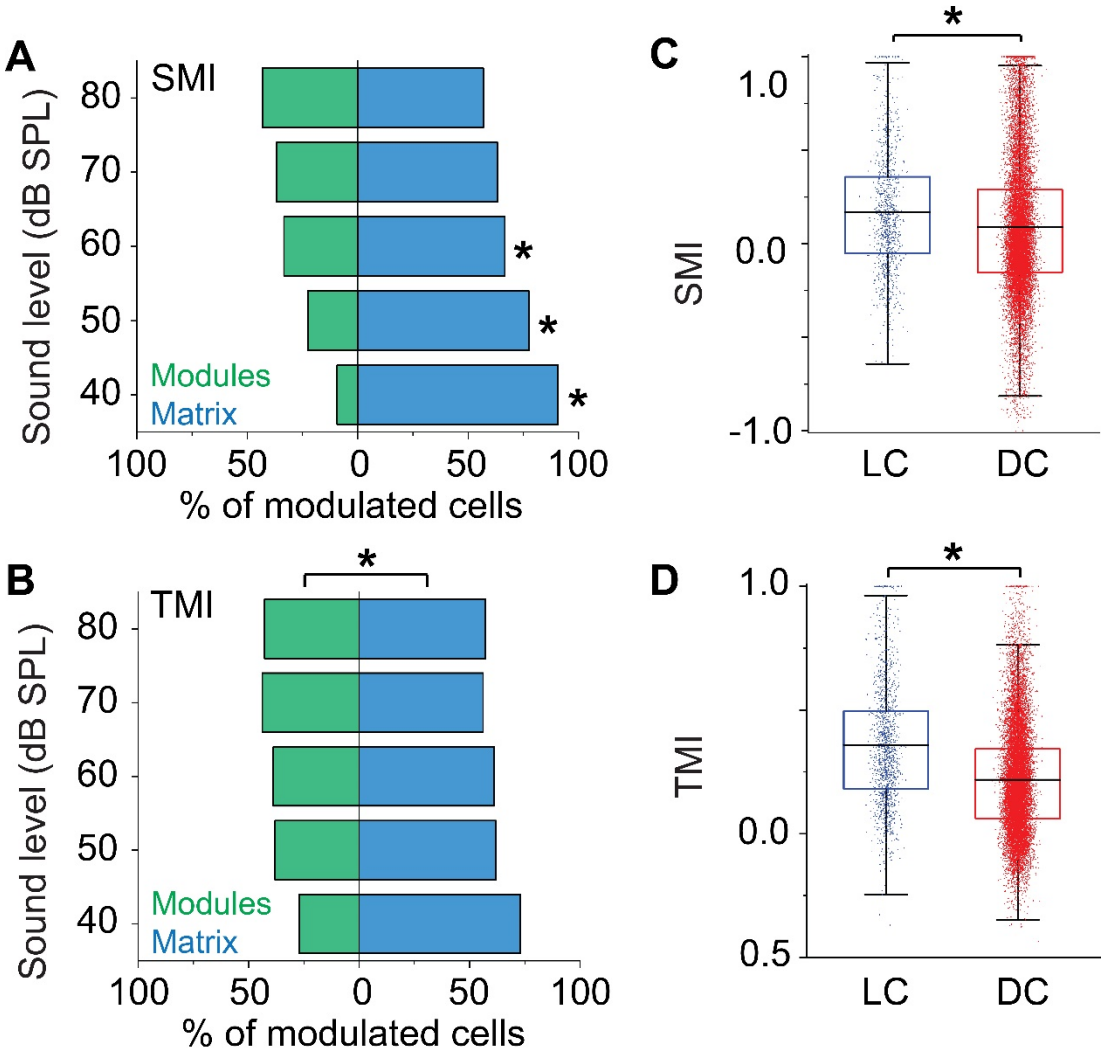

1111

1112

1113 Figure 8:

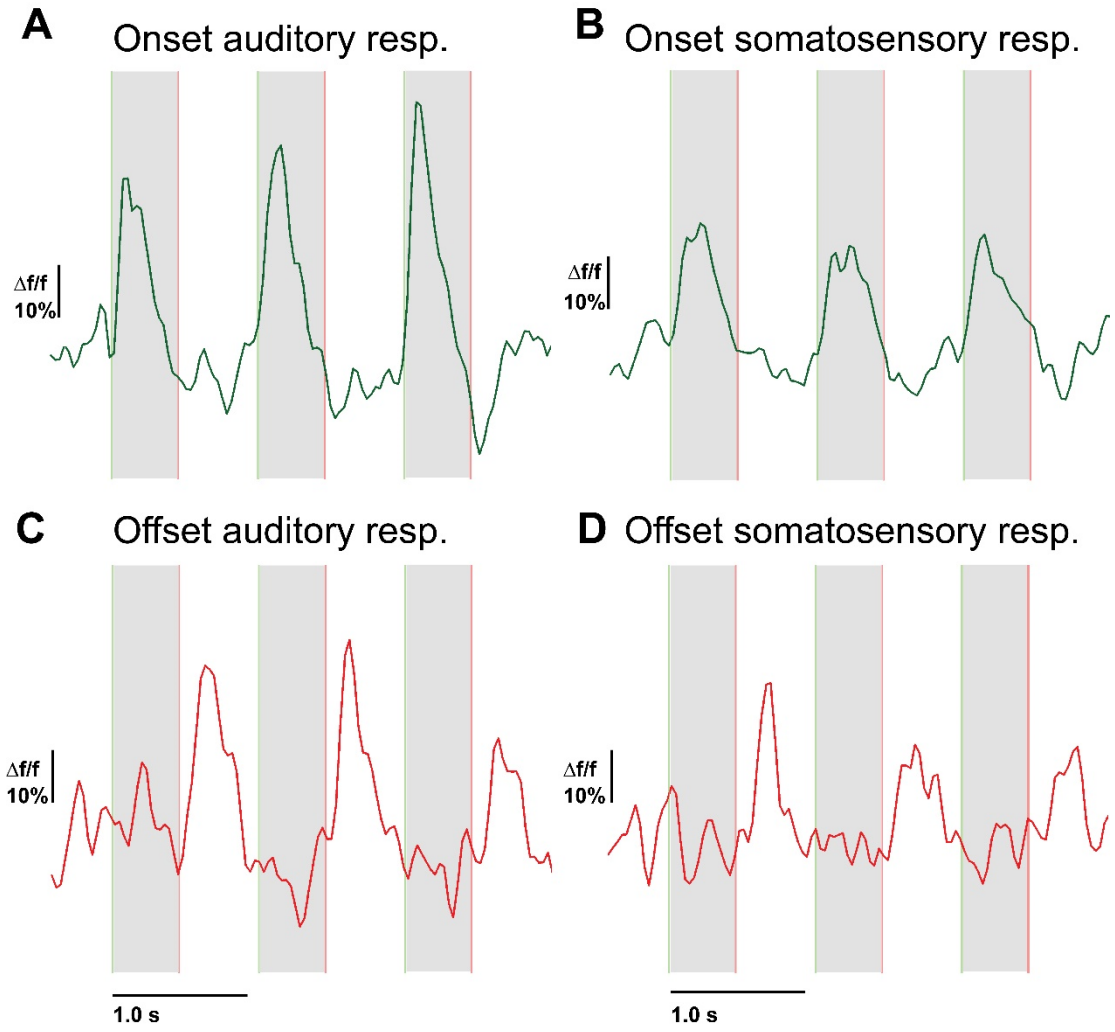

1114

1115

Figure 9:

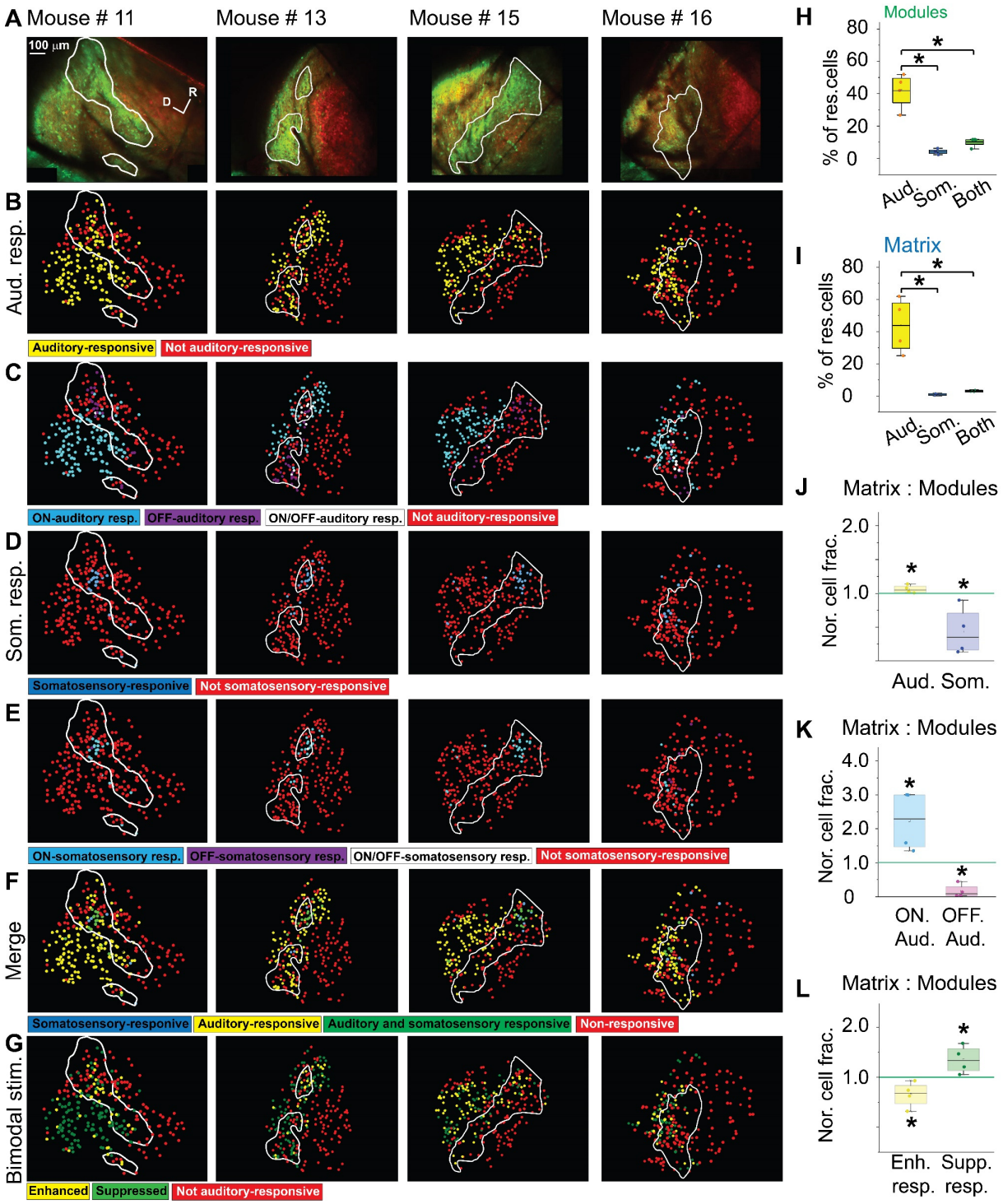
A Mouse # 11
Mouse # 13
Mouse # 15
Mouse # 16
100 µm
D
R
B
Aud. resp.
Auditory-responsive
Not auditory-responsive
C
ON-auditory resp.
OFF-auditory resp.
ON/OFF-auditory resp.
Not auditory-responsive
D
Som. resp.
Somatosensory-responive
Not somatosensory-responsive
E
ON-somatosensory resp.
OFF-somatosensory resp.
ON/OFF-somatosensory resp.
Not somatosensory-responsive
F
Merge
Somatosensory-responive
Auditory-responsive
Auditory and somatosensory responsive
Non-responsive
G
Bimodal stim.
Enhanced
Suppressed
Not auditory-responsive
H
Modules
% of res.cells
80
60
40
20
0
Aud.
Som.
Both
I
Matrix
% of res.cells
80
60
40
20
0
Aud.
Som.
Both
J
Matrix : Modules
Nor. cell frac.
2.0
1.0
Aud.
Som.
K
Matrix : Modules
Nor. cell frac.
4.0
3.0
2.0
1.0
0
ON. Aud.
OFF. Aud.
L
Matrix : Modules
Nor. cell frac.
2.0
1.0
Enh. resp.
Supp. resp.

Figure 10:

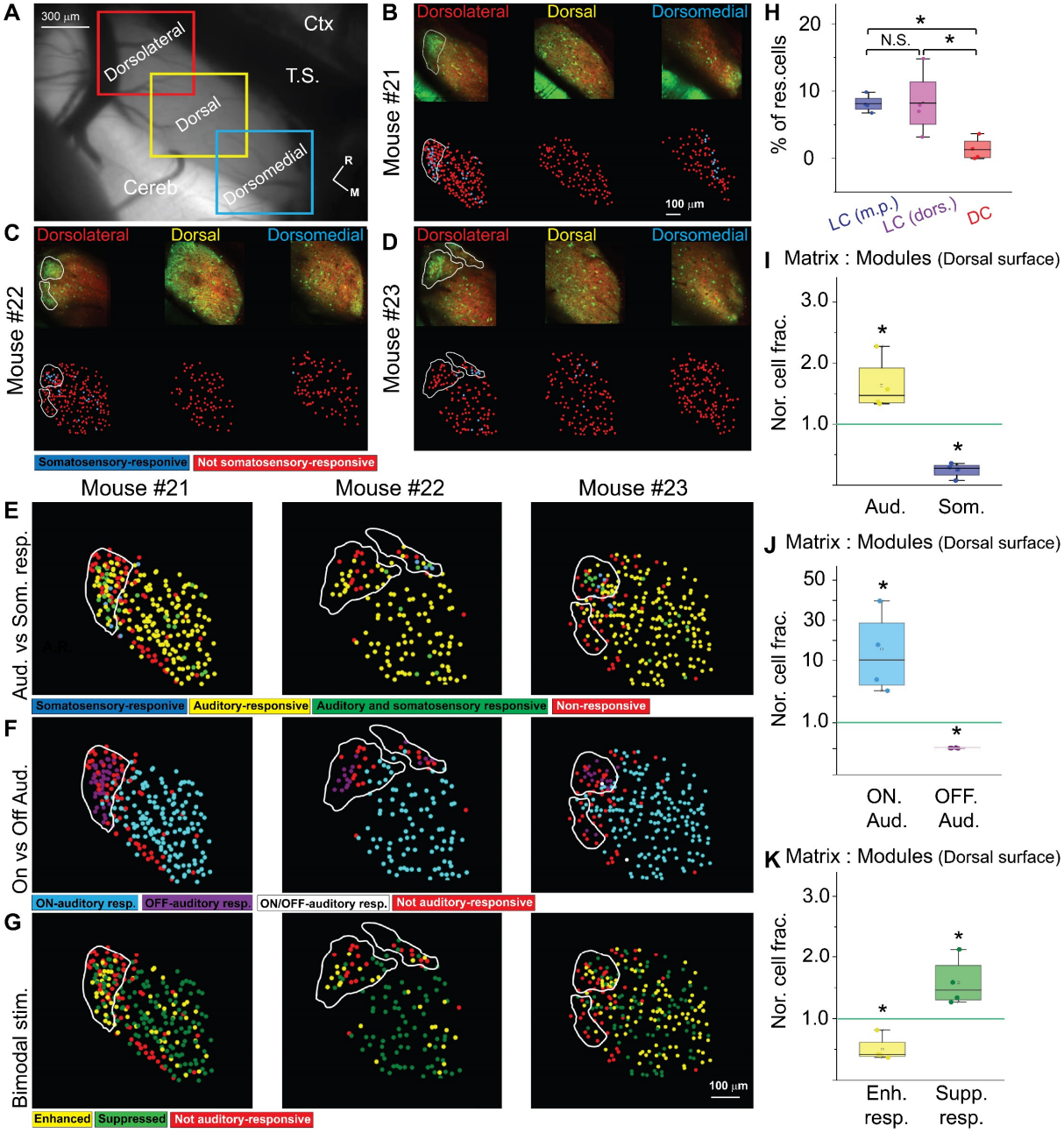
A
300 μm
Ctx
T.S.
Dorsolateral
Dorsal
Dorsomedial
Cereb
R
M
B
Mouse #21
Dorsolateral
Dorsal
Dorsomedial
100 μm
C
Mouse #22
Dorsolateral
Dorsal
Dorsomedial
D
Mouse #23
Dorsolateral
Dorsal
Dorsomedial
Somatosensory-responive
Not somatosensory-responsive
Mouse #21
Mouse #22
Mouse #23
E
Aud. vs Som. resp.
Somatosensory-responive
Auditory-responsive
Auditory and somatosensory responsive
Non-responsive
F
On vs Off Aud.
ON-auditory resp.
OFF-auditory resp.
ON/OFF-auditory resp.
Not auditory-responsive
G
Bimodal stim.
100 μm
Enhanced
Suppressed
Not auditory-responsive
H
% of res.cells
20
10
0
N.S.
*
*
LC (m.p.)
LC (dors.)
DC
I Matrix : Modules (Dorsal surface)
Nor. cell frac.
3.0
2.0
1.0
*
*
Aud.
Som.
J Matrix : Modules (Dorsal surface)
Nor. cell frac.
50
30
10
1.0
*
*
ON. Aud.
OFF. Aud.
K Matrix : Modules (Dorsal surface)
Nor. cell frac.
3.0
2.0
1.0
*
*
Enh. resp.
Supp. resp.

1122 Figure 11

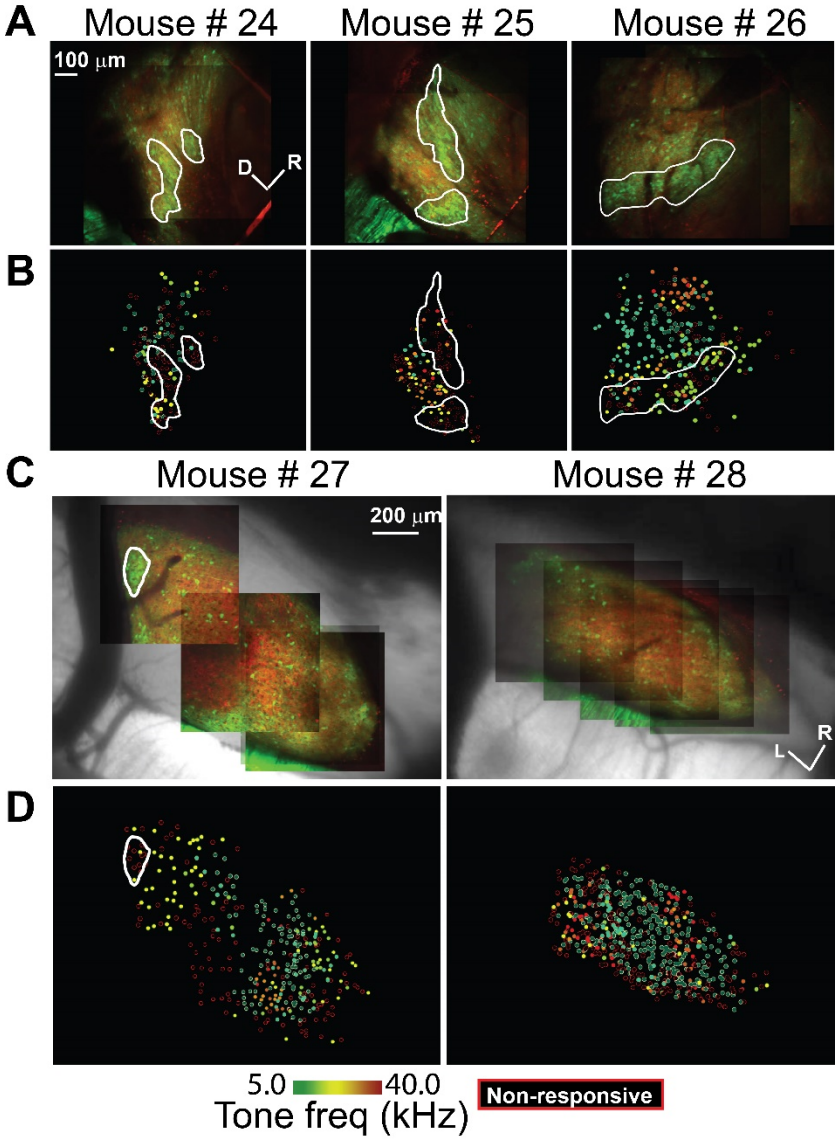

1123

1124

1125 Figure 12:

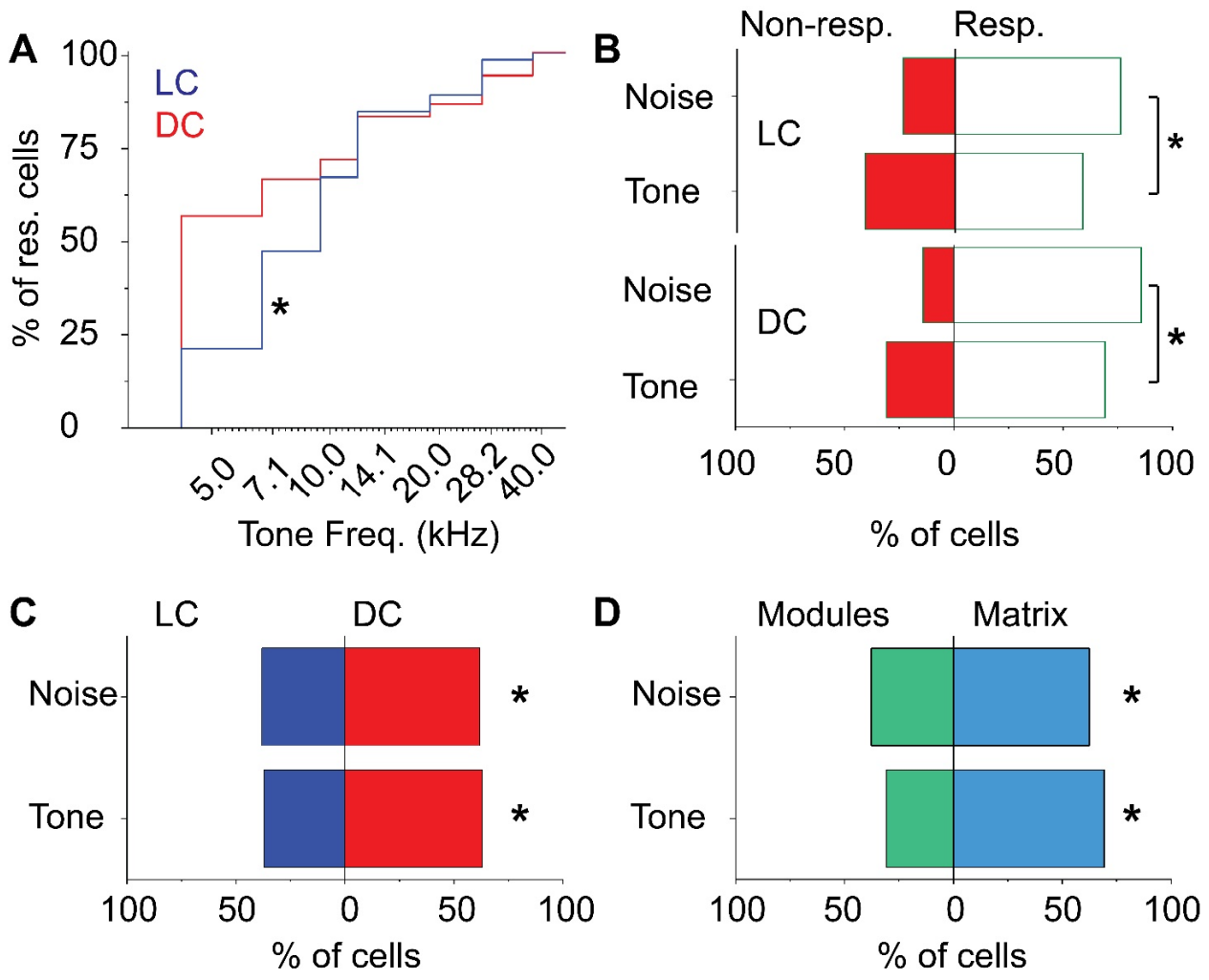

1126

1127

Figure 13:

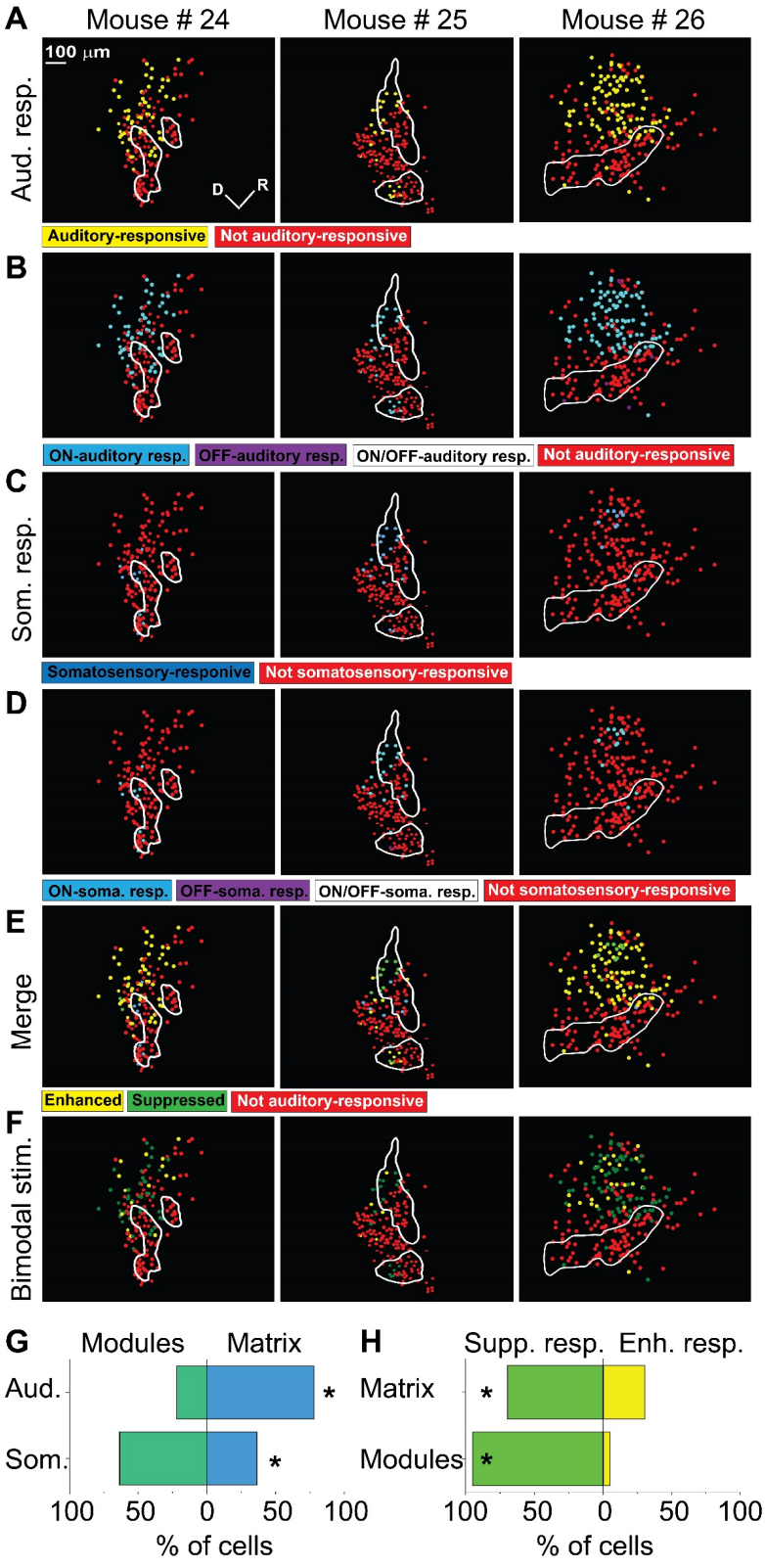
A
Mouse # 24
Mouse # 25
Mouse # 26
Aud. resp.
100 μm
D
R
Auditory-responsive
Not auditory-responsive
B
ON-auditory resp.
OFF-auditory resp.
ON/OFF-auditory resp.
Not auditory-responsive
C
Som. resp.
Somatosensory-responive
Not somatosensory-responsive
D
ON-soma. resp.
OFF-soma. resp.
ON/OFF-soma. resp.
Not somatosensory-responsive
E
Merge
Enhanced
Suppressed
Not auditory-responsive
F
Bimodal stim.
G
Modules
Matrix
Aud.
Som.
*
*
100
50
0
50
100
% of cells
H
Supp. resp.
Enh. resp.
Matrix
Modules
*
*
100
50
0
50
100
% of cells